Studies on Structures and Functions of Vitamin B[6] Degrading Enzymes(Dissertation_全文)

AUTHOR(S):

Kobayashi, Jun

Studies on

Structures and Functions of Vitamin B_6 Degrading Enzymes

Jun Kobayashi

2014

Contents

List of Abbreviations

AAH	α-(*N*-Acetylaminomethylene) succnic acid amidohydrolase
AAMHS	α-(*N*-Acetylaminomethylene)-β-hydroxymethyl succnic acid
AAMS	α-(*N*-Acetylaminomethylene) succnic acid
AHL	*N*-Acyl-homoserine lactone
ASU	Asymmetrical unit
DTT	Dithiothreitol
EDTA	Ethylene diamine tetraacetic acid
FAD	Flavinadeninedinucleotide
FAMS	α-(*N*-Formylaminomethylene) succnic acid
5HN	5-Hydroxynicotinic acid
HPLC	High-performance liquid chromatography
HSL	Homoserine lactone
iPL	iso-Pyridoxal
KPB	Potassium phosphate buffer
2ME	2-Mercaptoethanol
MHFPC	2-Methyl-3-hydroxy-5-formylpyridine-4-carboxylic acid
MHPC	2-Methyl-3-hydroxypyridine-5-carboxylic acid (5-Hydroxy-6-methylpyridine-3-carboxylic acid)
MHPCO	2-Methyl-3-hydroxypyridine-5-carboxylic acid oxygenase
MHPDC	2-Methyl-3-hydroxypyridine-4, 5-dicarboxylic acid
NAD(P)H	Nicotinamide adenine dinucleotide (phosphate)

4PA	4-Pyridoxic acid
5PA	5-Pyridoxic acid
4PAL	4-Pyridoxolactone
5PAL	5-Pyridoxolactone
PDB	Protein Data Bank
PEG	Polyethylene glycol
PL	Pyridoxal
PM	Pyridoxamine
PMSF	Phenylmethylsulfonylfluoride
PN	Pyridoxine
SAD	Single-wavelength anomalous dispersion
SDS-PAGE	Sodium dodecyl sulfate polyacrylamide gel electrophoresis
SeMet	Selenomethionine-substituted
SPB	Sodium phosphate buffer
TFE	2, 2, 2-Trifluoroethanol
WT	Wild-type
XAFS	X-ray absorption fine structure

List of PDB Accession Numbers

Selenomethionine-substituted 4-pyridoxolactonase	3AJ0
4-Pyridoxolactonase	4KEP
4-Pyridoxolactonase/5-pyridoxolactone complex	4KEQ
2-Methyl-3-hydroxypyridine-5-carboxylic acid oxygenase	4JY2
2-Methyl-3-hydroxypyridine-5-carboxylic acid oxygenase/5-pyridoxic acid complex	4JY3

General Introduction

A limited number of soil microorganisms have vitamin B_6 degradation pathway to assimilate vitamin B_6. Two pathways have been discovered by Snell *et al.* (*1*). Pathway I was discovered in *Pseudomonas* sp. MA-1 and is consisted of nine enzymes (Scheme 1, left). Pathway II was discovered in *Pseudomonas* IA and *Arthrobacter* Cr-7, and is consisted of five enzymes (Scheme 1, right). In the pathway I, there are enzymes which have unique catalytic mechanisms (1'st, 5th, 6th, 7th and 8th enzymes) and metabolic intermediates which have useful activity for industrial application, for example, a therapeutic potential of diabetic complication (pyridoxamine; PM), antimicrobial activity (pyridoxal; PL, 4-pyridoxolactone; 4PAL) and biomarkers of metabolism of vitamin B_6 (4-pyridoxic acid; 4PA) and Alzheimer's disease (2-methyl-3-hydroxypyridine-5-carboxyic acid; MHPC) in human.

Based on these academic and industrial interest, enzymatic properties of all nine and five enzymes have been partially characterized (*2-12*). Recently, the pathway I has been discovered in, a symbiotic nitrogen-fixing bacterium, *Mesorhizonium loti* by Yagi *et al*. (*13*). Enzymes in the pathway I from *M. loti* have enzymatically been characterized (*13-19*). Following these enzymatic approaches, the crystal structures of pyridoxamine-pyruvate aminotransferase (1'st), pyridoxal 4-dehydrogenase (2nd) and 2-methyl-3-hydroxy-pyridine-4, 5-dicarboxylic acid decarboxylase (6th) have been determined and their catalytic mechanisms have been discussed (*20-22*). In this thesis, following these studies, the crystal structures of 4-pyridoxolactonase (3rd), 2-methyl-3-hydroxypyridine-5-carboxylic acid oxygenase (MHPCO, 7th) and α-(*N*-acetylaminomethylene) succinic

acid amidohydrolase (AAH, 8th) in the pathway I from *M. loti* were determined to elucidate correlations between the structures and functions.

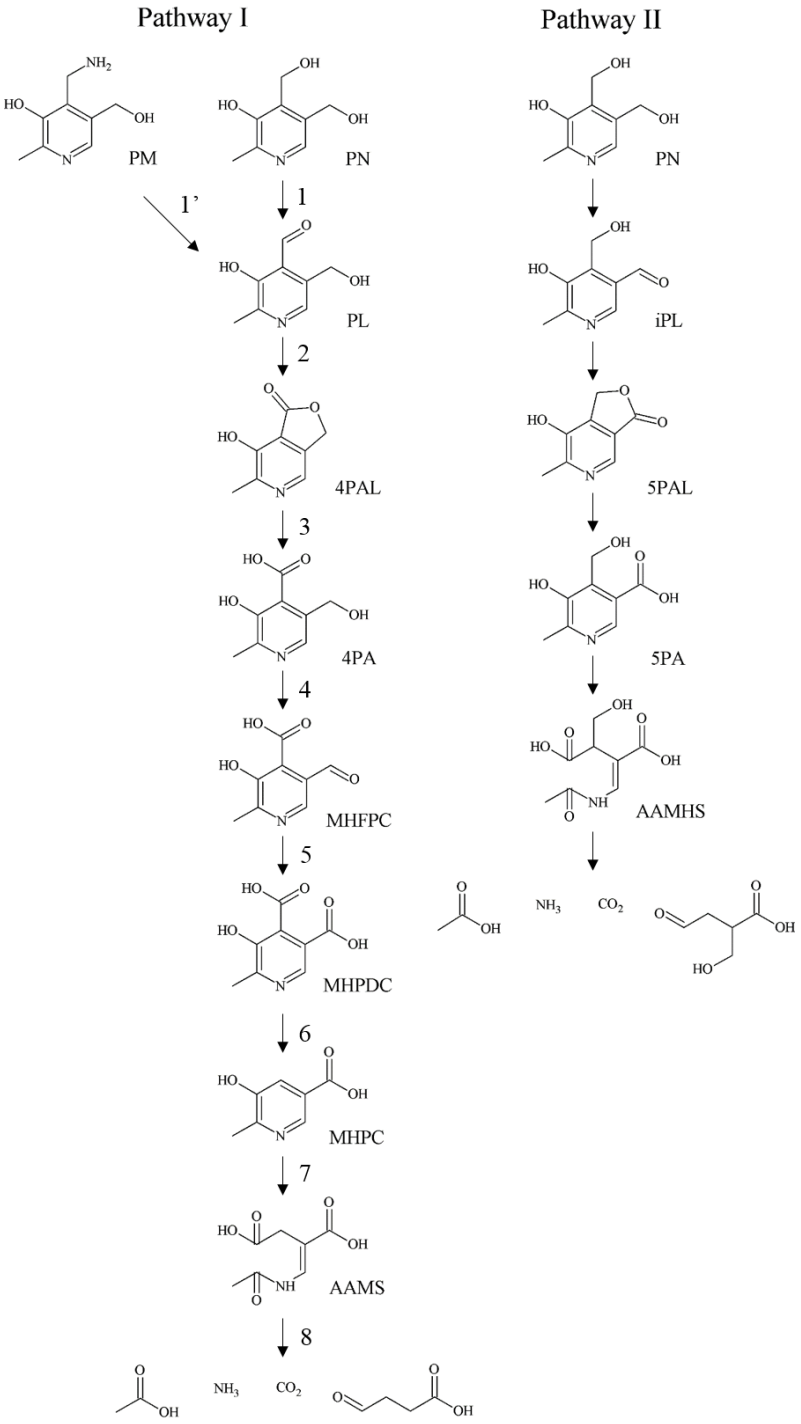

Scheme 1. Vitamin B_6 degradation pathway I and II.

4-Pyridoxolactonase catalyzes the Zn-dependent lactone-ring hydrolysis of 4PAL to 4PA (Scheme 1). The enzymatic property of the enzyme from *M. loti* has been reported and it belongs to the class B β-lactamase (*15*). However, the crystal structure and catalytic mechanism have not been elucidated. In Chapter 1, I described the structural feature of 4-pyridoxolactonase. Furthermore, I described the catalytic mechanism, based on the crystal structures of the enzyme and its complex with a competitive inhibitor, 5-pyridoxolactone (5PAL, a compound in the pathway II, Scheme 1) and docking simulations with 4PAL, 4PA and a reaction intermediate.

2-Methyl-3-hydroxypyridine-5-carboxylic acid oxygenase (MHPCO) catalyzes the FAD-dependent pyridine-ring opening reaction of MHPC to α-(*N*-acetylamino-methylene) succinic acid (AAMS) (Scheme 1). This reaction adds two oxygen atoms to MHPC and then cleaves the pyridine-ring in the presence of FAD, NADH, molecular oxygen and water. MHPCO also acts as an inefficient NAD(P)H oxidase in the absence of MHPC, as found in other NAD(P)H-dependent flavoenzymes (*8*). In these ring-opening and NAD(P)H oxidation activities, an interesting property has been observed: the reduction rate of FAD by NADH is enhanced several-thousand-fold in the presence of MHPC, although MHPC is not directly involved in the reduction (*23*). In Chapter 2, I described the mechanism of this "effector role of substrate" based on the crystal structures of MHPCO, MHPCO/5-pyridoxic acid (5PA, an alternative substrate and a compound in the pathway II, Scheme 1) complex, site-directed mutagenesis in Tyr270 (Y270F and Y270A mutants) and enzyme kinetics of the WT and mutants in the presence or absence of a substrate.

α-(*N*-Acetylaminomethylene) succinic acid amidohydrolase (AAH) catalyzes the degradation of AAMS to acetate, ammonia, carbon dioxide and succinic

semialdehyde (Scheme 1). The enzymatic property of AAH from *M. loti* has been reported and the catalytic residues are thought to be Ser-His-Asp observed in various hydrolases (*19*). The primary structure of the enzyme shows low but significant identities (~30%) to several dehalogenases and esterases. However, the corresponding Asp residue could not be predicted from sequence alignment with them. Therefore, the catalytic residues have not been elucidated. In Chapter 3, I described the structural feature and catalytic residues of AAH. Furthermore, I mentioned a presence of a new subclass in the α/β hydrolase superfamily to which AAH belongs.

References

1. Burg, W. R., Rodwell, W. V., and Snell, E. E. (1959) *J. Biol. Chem.* **235**, 1164-1169.
2. Sundaram, K. T., and Snell, E. E. (1969) *J. Biol. Chem.* **244**, 2577-2584.
3. Dempsey, W. B., and Snell, E. E. (1963) *Biochemistry* **2**, 1414-1419.
4. Burg, R. W., and Snell, E. E. (1969) *J. Biol. Chem.* **244**, 2585-2589.
5. Yagi, T., Kishore, G. M., and Snell, E. E. (1983) *J. Biol. Chem.* **258**, 9419-9425.
6. Lee, Y. C., Nelson, M. J., and Snell, E. E. (1986) *J. Biol. Chem.* **261**, 15102-15105.
7. Snell, E. E., Smucker, A. A., Ringermann, E., and Lynen, F. (1964) *Biochem. Z* **341**, 109-119.
8. Sparrow, L. G., Ho, P. P., Sundaram, T. K., Zach, D., Nyns, E. J., and Snell, E. E. (1969) *J. Biol. Chem.* **244**, 2590-2600.
9. Nyns, E. J., Zach, D., and Snell, E. E. (1969) *J. Biol. Chem.* **244**, 2601-2605.
10. Jong, Y. J., and Snell, E. E. (1986) *J. Biol. Chem.* **261**, 15112-15114.
11. Nelson, M. J., and Snell, E. E. (1986) *J. Biol. Chem.* **261**, 15115-15120.
12. Huynh, M. S., and Snell, E. E. (1985) *J. Biol. Chem.* **260**, 2379-2383.

13. Yuan, B., Yoshikane, Y., Yokochi, N., Ohnishi, K., and Yagi, T. (2004) *FEMS Microbiol. Lett.* **234**, 225-230.

14. Yokochi, N., Nishimura, S., Yoshikane, Y., Ohnishi, K., and Yagi, T. (2006) *Arch. Biochem. Biophys.* **452**, 1-8.

15. Funami, J., Yoshikane, Y., Kobayashi, H., Yokochi, N., Yuan, B., Iwasaki, K., Ohnishi, K., and Yagi, T. (2005) *Biochim. Biophys. Acta* **1753**, 234-239.

16. Ge, F., Yokochi, N., Yoshikane, Y., Ohnishi, K., and Yagi, T. (2008) *J. Biochem.* **143**, 603-609.

17. Yokochi, N., Yoshikane, Y., Matsumoto, S., Fujisawa, M., Ohnishi, K., and Yagi, T. (2009) *J. Biochem.* **145**, 493-503.

18. Yuan, B., Yokochi, N., Yoshikane, Y., Ohnishi, K., and Yagi, T. (2006) *J. Biosci. Bioeng.* **102**, 504-510.

19. Yuan, B., Yokochi, N., Yoshikane, Y., Ohnishi, K., Ge, F., and Yagi, T. (2008) *J. Nutri. Sci. Vitaminol. (Tokyo)* **54**, 185-190.

20. Yoshikane, Y., Yokochi, N., Yamasaki, M., Mizutani, K., Ohnishi, K., Mikami, B., Hayashi, H., and Yagi, T. (2008) *J. Biol. Chem.* **283**, 1120-1127.

21. Chu, H. N., Kobayashi, J., Mikami, B., and Yagi, T. (2011) *Biosci. Biotechnol. Biochem.* **75**, 388-390.

22. Mukherjee, T., McCulloch, K. M., Ealick, S. E., and Begley, T. P. (2007) *Biochemistry* **46**, 13606-13615.

23. Chayien, P. (2009) *Arch*. *Biochem*. *Biophys*. **493**, 62-70.

Chapter 1

Crystal Structure of 4-Pyridoxolactonase

Introduction

4-Pyridoxolactonase catalyzes the Zn-dependent lactone-ring hydrolysis of 4PAL (Scheme 1) to 4PA. The enzymatic property of 4-pyridoxolactonase from *M. loti* has been reported (*1*): The enzyme is a homodimeric protein with a molecular weight of 59,000 (subunit: 31,000), and exhibits K_m and k_{cat} values of 8.0 μM and 12 s^{-1}, respectively. 5PAL acts as the competitive inhibitor with K_i value of 150μM (Scheme 1). The enzyme belongs to the class B β-lactamase (as known as the metallo-β-lactamase superfamily) from the primary structure (~30% identity).

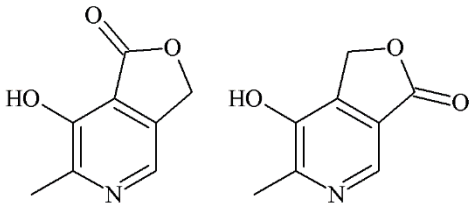

Scheme 1. Chemical structures of 4PAL and 5PAL.

Members of the class B β-lactamase are divided into three subclasses according to coordination manners and affinities for zinc ion in the active site (*2-4*). Subclass B1 enzymes need one or two zinc ions for their activity. The affinity of one binding site is higher than the other, and dizinc enzyme shows a higher activity than monozinc one. They share a consensus sequence, HXHXD~H~C~H. Although subclass B2 enzymes require one zinc ion for their activity, they have two zinc binding sites. Binding of the second

zinc ion inactivates the B2 enzymes. They share a consensus sequence, NXHXD~H~C~H. Subclass B3 enzymes need two zinc ions for their activity. Both binding sites have high affinities for zinc, and they are inactive in monozinc form. They share a consensus sequence, HXHXDH~H~H.

Several catalytic mechanisms have been proposed for the subclasses (*4*). For the subclass B1 and B3 enzymes coordinated to two zinc ions (Zn1 and Zn2): (i) a β-lactam substrate binds to an active site, where the carbonyl oxygen of the substrate interacts with Zn1. This interaction further polarizes the carbonyl group of the substrate. The lactone oxygen of the substrate interacts with Zn2. (ii) A hydroxide ion (an activated water molecule) between the two zinc ions attacks the positively-polarized carbonyl carbon of the substrate. This nucleophilic attack by the hydroxide ion creates a tetrahedral intermediate. (iii) The C-N bond of the tetrahedral intermediate is cleaved to form an anionic nitrogen intermediate and the anionic nitrogen interacts with Zn2. This interaction stabilizes the anionic intermediate. (iv) The anionic nitrogen intermediate readily forms a ring-opened product.

For the subclass B2 enzymes coordinated to one zinc ion (this zinc ion corresponds to Zn2 in the subclass B1 and B3), a similar mechanism by His and Asp residues instead of Zn1 has been proposed (*4*). Furthermore, another catalytic mechanism has been proposed for a subclass B2 enzyme (*5*): the same tetrahedral intermediate is formed through a similar pathway of (i) and (ii) by Zn2 and a hydroxide ion. (iii) A dianionic tetrahedral intermediate is formed by a proton transfer between the tetrahedral intermediate and Asp residue in the active site. Zn2 stabilizes the dianionic intermediate by interacting with both anions. (iv) Finally, the same product is readily formed. Although 4-pyridoxolactonase belongs to the class B β-lactamse (*1*), the coordination manner of

zinc ion and the catalytic mechanism have not been elucidated.

A preliminary X-ray crystallographic analysis of 4-pyridoxolactonase from *M. loti* has been recently reported (*6*). However, the crystal structure has not been elucidated owing to the phase problem. In this chapter, I determined the crystal structure of selenomethionine-substituted (SeMet) 4-pyridoxolactonase from *M. loti* by the single-wavelength anomalous dispersion method using selenium (Se-SAD method). I also determined the structures of the native 4-pyridoxolactonase and its 5PAL complex. Furthermore, I obtained the binding models of 4PAL, 4PA and a dianionic intermediate by docking simulation. Based on these results, I describe the structural feature, competitive inhibition mechanism by 5PAL and catalytic mechanism of 4-pyridoxolactonase.

Materials and Methods

Bacterial strains, plasmids and reagents

A bacterial strain and reagents reported previously were used (*1*). But, the expression plasmid vector of 4-pyridoxolactonase, pET21a6805 was engineered in order to add His_6-tag in the C-terminal of the enzyme. The plasmid of 4-pyridoxolactonase-His_6, pET21a6805-H_6 was prepared by using KOD -Plus- Mutagenesis Kit (TOYOBO) according to the instruction manual. The primers were 5'-CATATGTCGGATACAAAGGTCTACCTGCTCGAC-3' and 5'-AAGCTTTCAGTG GTGGTGGTGGTGGTGGCCGTAGAATTGCGTGCCGGTC-3', respectively.

Expression of the native and SeMet 4-pyridoxolactonase-His_6

The method used to induce the expression of the native 4-pyridoxolactonase-

His_6 was the same as that of the native enzyme without a His_6-tag reported previously (*1*), but the culture time was set at 48 hr. The SeMet 4-pyridoxolactonase-His_6 was expressed using *Escherichia coli* B834 (DE3) cells transformed by the two vectors, pET21a6805-H_6 and pKY206 containing chaperonine Gro EL/ES chaperonine genes (*7*). The cell colony was cultured with 5 ml LB medium containing two antibiotics (50 μg/ml ampicillin and 12.5 μg/ml tetracycline) for 12 hr at 37ºC, and then washed twice by SeMet core medium (Wako). The washed cells were cultured with 200 ml SeMet core medium containing 1% (w/v) glucose, 0.0025% (w/v) $MgSO_4 \cdot 7H_2O$, 0.0004175% (w/v) $FeSO_4 \cdot 7H_2O$, 50 mg/l seleno-L-methionine and the antibiotics at 23ºC. When OD_{500} reached 0.5, 0.5 mM IPTG was added. The cells were collected after 36 hr at 23ºC.

Enzyme and protein assay

The activity of 4-pyridoxolactonase was assayed by measuring the decrease in the absorbance of 4PAL (356nm) as reported by Funami *et al*. (*1*). The protein concentration was measured by a Bio-Rad Protein Assay (Bio-Rad) using bovine serum albumin as a standard. The concentration of purified 4-pyridoxolactonase was determined from the molecular absorption coefficient (ε = 51,990 M^{-1} cm^{-1}) at 280 nm (*1*).

Purification

The native and SeMet 4-pyridoxolactonase-His_6 were purified by the same method. The harvested cells were suspended in Buffer A [20 mM potassium phosphate buffer (KPB) (pH 7.5), 14 mM 2-mercaptoethanol (2ME), 10% (w/v) glycerol, 20 mM imidazole, 300 mM NaCl] and then sonicated for 5 min on ice. A crude extract was obtained by centrifugation at 8000 g for 10 min at 4ºC. The crude extract was immediately

applied onto an Ni-NTA agarose (QIAGEN) column chromatography. The column was equilibrated with Buffer A, and then the crude extract was applied. The column was washed with Buffer A containing 50 mM imidazole, and then proteins bound to the column were eluted by a linear gradient of 50 - 500 mM imidazole. The fractions showing 4-pyridoxolactonase activity eluted at around 200 mM imidazole. The fractions were collected and then the buffer was changed to Buffer B [20 mM Tris-HCl (pH 7.5), 14 mM 2ME, 10% glycerol] using a VIVASPIN 20 (10,000 MWCO, Saltorius Stedim Biotech). The sample was also applied onto a hydroxyapatite column chromatography. The column was equilibrated with Buffer B and then the sample was applied. The column was washed with Buffer B and then proteins bound were eluted by a linear gradient of 0 - 50 mM KPB. The fractions with the 4-pyridoxolactonase activity were eluted at around 20 mM KPB. The fractions were further applied onto a Shodex protein KW-803 (SHOWADENKO) gel filtration column chromatography using crystallization buffer [10 mM HEPES-Na (pH 7.5), 10% glycerol, 3 mM tris (2-carboxyethyl) phosphine-HCl]. Fractions containing proteins around 60,000 Da which correspond to the 4-pyridoxolactonase dimer were collected and used for crystallization.

Crystallization and structure determination

The purified native-His_6 and SeMet-His_6 enzymes were concentrated to 8 mg/ml by ultra-filtration using a VIVASPIN 20. The native enzyme without the His_6-tag has already been crystallized using reservoir solution [30% (w/v) PEG4000, 200 mM ammonium acetate and 100 mM sodium acetate] (*6*). After optimization, both the native-His_6 and SeMet-His_6 enzymes were crystallized by mixing the equal volumes (2 µl: 2 µl) of the enzyme solution (8 mg/ml in crystallization buffer) and reservoir solution [30%

(w/v) PEG4000, 150 mM ammonium acetate and 100 mM sodium acetate] by the sitting drop method for one month at 4ºC. The native-His_6/5PAL complex was not crystallized under this condition. After screening with Crystal Screen I and II (Hampton Research) and Wizard I and II (Emerald Biosystems) and further optimization, a crystal was obtained by mixing equal volumes (1 µl: 1 µl) of enzyme solution (8 mg/ml and 5 mM 5PAL in the crystallization buffer) and reservoir solution [20% (w/v) PEG3350 and 50 mM ammonium citrate, pH 5.1] by the sitting drop method for three months at 4ºC.

All diffraction data were collected at SPring-8 (Hyogo, Japan). The crystals were flash-cooled directly in a liquid nitrogen stream. The data for the SeMet crystal were collected by a sagittal light collection system at BL38B1. A wavelength was set at 0.97800 Å from X-ray absorption fine structure (XAFS) measurements, and the crystal-to-detector distance was set at 150.0 mm. Oscillation images of 0.7º were collected with an exposure time of 6 s. Data for the native-His_6 and native-His_6/5PAL complex crystals were collected using a normal light collection system. For the native-His_6 and its 5PAL complex crystals, the wavelengths was set to 1.000 and 0.9000 Å, and the crystal-to-detector distance was set to 250 and 270 mm, respectively. Oscillation images of 1º and 1º were collected with exposure times of 4 and 2.5 s, respectively. All data were processed by HKL2000 (*8*). The data collection statistics are shown in Table I.

The crystal structure of the SeMet-His_6 enzyme was determined by the Se-SAD method. Four selenium sites were identified by SHELXD, and the initial phase was determined by SHELXE (*9*). The density modification (*10*) and model building (*11*) were performed using RESOLVE. The structure was refined to 1.58 Å by PHENIX (*12*) and COOT (*13*). The initial phases of the native-His_6 and native-His_6/5PAL complex structures were determined by a molecular replacement method with MOLREP (*14*) in

CCP4 (*15*) using the SeMet structure as a template. Refinement and modeling of both structures were performed by REFMAC5 (*16*), PHENIX and COOT. The model of 5PAL was generated by PRODRG (*17*). All final structures and structure factors were evaluated by PROCHECK (*18*) and SFCHECK (*19*), respectively. These refinement statistics are shown in Table I. The structural similarity was conducted using DALI (*20*). Interaction areas of the enzymes in crystal form were calculated using PISA (*21*). The crystal structures and structure factors have been deposited in Protein Data Bank (PDB) as entries 4KEP (the native-His_6), 3AJ3 (SeMet-His_6) and 4KEQ (native-His_6/5PAL complex).

Table I. Data collection and refinement statistics.

	SeMet-His_6 (3AJ3)	Native-His_6 (4KEP)	Native-His_6 + 5PAL (4KEQ)
Data collection			
X-ray source	SPring-8 BL38B1		SPring-8 BL44XU
Wavelength (Å)	0.97800	1.0000	0.9000
Crystal system	Monoclinic	monoclinic	monoclinic
Space group	*C*2	*C*2	*C*2
Unit cell parameter (Å,°)	*a* = 82.777,	*a* = 84.751,	*a* = 84.737,
	b = 39.214,	*b* = 39.198,	*b* = 39.557,
	c = 84.191,	*c* = 84.200,	*c* = 84.564,
	β = 117.92	β = 117.68	β = 117.69
Resolution limit (Å)	28.99-1.58 (1.64-1.58)	50-1.83 (1.86-1.83)	50-2.28 (2.32-2.28)
Measured reflections	217995 (16621)	133238 (6678)	47918 (2124)
Unique reflections	32428 (3078)	21861 (1113)	11493 (559)
Redundancy	6.7 (5.4)	6.1 (6.0)	4.2 (3.8)
Completeness (%)	97.8 (93.0)	99.8 (99.7)	99.6 (98.8)
$\langle I/\sigma(I)\rangle$	22.6 (7.90)	19.7 (5.65)	30.3 (12.7)
R_{merge} (%)	5.1 (28.4)	5.3 (40.5)	7.8 (22.8)
Refinement			
Resolution range (Å)	28.99-1.58 (1.63-1.58)	36.1-1.83 (1.91-1.83)	36.2-2.28 (2.51-2.28)
R_{work} (%)	16.3 (18.9)	17.5 (19.5)	18.8 (20.4)
R_{free} (%)	19.0 (22.0)	20.9 (25.8)	24.6 (29.2)
Amino acid residue	273	273	269
Zn	2	2	2
5PAL	-	-	2
Acetate	-	1	-
Water	325	90	41
B-factor ($Å^2$)			
Protein	16.49	29.03	22.42
Water	25.36	29.23	19.75
Zn1 / Zn2	30.21 / 14.32	20.76 / 21.62	20.00 / 19.67
Acetate	-	29.01	-
5PAL in the active site	-	-	21.47

Values in parentheses are for the highest resolution shell.

Docking simulation

Docking simulations of 4-pyridoxolactonase with 4PAL (substrate), 4PA (product) or a dianion intermediate (a reaction intermediate) were performed by using AutoDock 4.2 (*22*). The models of 4PAL, 4PA and the dianion intermediate were generated by PRODRG (*17*). The model of 4-pyridoxolactonase was prepared from the structure of 4-pyridoxolactonase/5PAL complex. All water molecules and ligands in the 4-pyridoxolactonase model were removed except for the catalytic water and two zinc ions in the active site. Hydrogen atoms and partial charges were added by AutoDockTools-1.5.6. Glu65, Phe99, Leu132, Phe223 in the active site were set to be flexible. The docking site was defined by a grid box 40 × 40 × 40 points and spacing of 0.375 Å with the 5PAL binding site as the center. The docking was done with Lamarckian genetic algorithm with population size of 150. 30 independent docking trials were performed for each compound.

Results and Discussion

Expression and purification

The native-His_6 and SeMet-His_6 enzymes were expressed in *E. coli*. The expression levels were almost the same (~10% in the crude extracts by SDS-PAGE densitogram). Both enzymes were purified to homogeneity by Ni-NTA, hydroxyl apatite and gel filtration column chromatography. The native-His_6 and SeMet-His_6 enzymes showed the same retention time on gel filtration column chromatography. The purified native-His_6 enzyme showed almost the same activity (~120%) as the purified native enzyme without a His_6-tag, but the SeMet-His_6 enzyme showed an extremely low activity (0.24% of the native enzyme without a His_6-tag).

Crystal structure

The crystal structure of the SeMet-His_6 enzyme was determined and refined to 1.58 Å. The crystal structures of the native-His_6 enzyme and native-His_6/5PAL complex were also determined by the molecular replacement method and refined to 1.83 and 2.28 Å, respectively. Ramachandran plots (*23*) by PROCHECK (*18*) of the SeMet-His_6, native-His_6 and native-His_6/5PAL complex structures showed that 87.7, 88.4 and 84.7% of amino acid residues existed in most favored region, 10.9, 10.3 and 14.0% in additional allowed region, 0.5, 0.9 and 0.4% in generously allowed region and 0.9, 0.4 and 0.9% in disallowed region, respectively.

Although 4-pyridoxolactonase from *M. loti* exists as a dimer in solution (*1*), a monomer was found in the asymmetrical unit. The monomer interacted with a monomer related by a crystallographic twofold axis through residues 17-28, 127-129 and 217-235 to form a dimer (Fig. 1a, b). This dimer formed C-C contacts between Trp23 and Phe129* and between Phe129 and Trp23* (4.0 Å). The dimer also formed four intermolecular hydrogen bonds between Nε2 o His20 and O of Asn24* (3.0 Å), between Nε1 of Trp23 and O of Ala222* (2.8 Å), between O of Asn24 and Nε2 of His20* and between O of Ala222 and Nε1 of Trp23, respectively. The buried solvent-accessible surface area per monomer by this dimerization was ~790 $Å^2$ (6.6% of the whole area). Because 368-4746 $Å^2$ is considered to be reasonable for formation of a functional dimer (*24*). Although further mutational analysis is needed, this dimer (~1580 $Å^2$) seems to be a functional dimer in the solution phase.

The overall structure of 4-pyridoxolactonase monomer was an αβ/βα sandwich fold (Fig. 1c, d): it consisted of central six-stranded and five-stranded mixed β-sheets, and 13 α-helices which sandwiched the two β-sheets. No major structural difference was

observed among the structures of the SeMet-His_6, native-His_6 and native-His_6/5PAL complex (RMSD < 0.2 Å). A similarity search with the DALI server indicated that 4-Pyridoxolactonase showed high similarities to Zn-dependent *N*-acyl-homoserine lactone (AHL) lactonase AiiB from *Agrobacterium tumefaciens* (PDB ID: 2R2D, Z-score = 32.6, RMSD = 1.7 Å) (*25*), Zn-dependent AHL lactonase AiiA from *Bacillus thuringiensis* (3DHB, 31.8, 1.8 Å) (*26*) and methyl parathion hydrolase from *Pseudomonas* sp. WBC-3 (1P9E, 22.8, 2.4 Å), respectively. The enzyme also showed slight similarities to IMP-1 (belongs to the subclass B1), VIM-4 (B1), VIM-2 (B1), AIM-1 (B3), FEZ-1 (B3), NDM-1 (B1), L1 (B3) β-lactamase (Z-score ~15, RMSD ~3 Å). All enzymes belonged to the class B β-lactamase, and their fold type was the αβ/βα sandwich fold.

The active site of 4-pyridoxolactonase was located at the top of the central β-sheets, and two zinc ions were coordinated (Fig. 2). One zinc ion (Zn1) was coordinated by Nε2 of His96, Nδ1 of His98, Nε2 of His185, Oδ2 of Asp207 and an acetate molecule that was probably from the crystallization solution. The other (Zn2) was coordinated by Oδ2 of Asp100, Nε2 of His101, Oδ2 of Asp207, Nε2 of His252 and the same acetate molecule. Although one acetate molecule was the ligand of the zinc ions in the native structure (Fig. 2a and 2b), two water molecules were the ligands in the SeMet structure (Fig. 2c). In other dinuclear zinc enzymes, the distance between Zn1 and Zn2 was ranged from 3.5 to 4.4 Å (*2, 27*). In the 4-pyridoxolactonases with the native-His_6, native-His_6/5PAL or SeMet-His_6 structures, the distances between the two ions was also 3.5 Å. In the SeMet-His_6 enzyme, the electron density of Zn1 was too weak to distinguish the nature of the molecule. When the density was modeled as Zn1, the occupancy was low (occupancy = 0.23). Therefore, the low activity of the SeMet-His_6 enzyme (0.24% of that of the native enzyme) was probably attributed to the low occupancy of Zn1 in the active

site. This low occupancy was probably due to a limited amount of zinc in the SeMet core medium. Thus, active 4-pyridoxolactonase coordinated and required two zinc ions, and the manner of coordination was $H^{96}FHFDH^{101}$~H^{185}~H^{252}, with the additional coordination of Asp^{207}. These results strongly suggested that 4-pyridoxolactonase belongs to the subclass B3 of the class B β-lactamase (*4*).

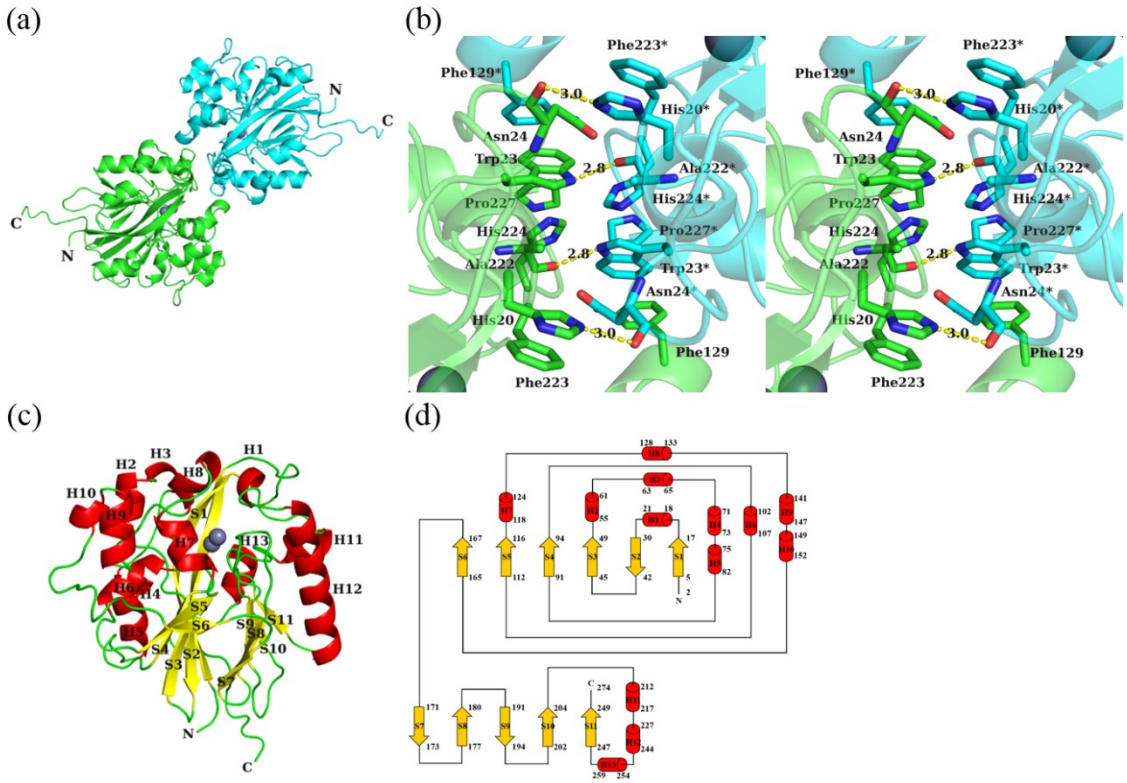

Figure 1. The crystal structure of 4-pyridoxolactonase. (a) A crystallographic dimer. The monomers are colored green and cyan. N- and C-terminals are labeled N and C, respectively. Zinc ions are shown as gray spheres. (b) The dimeric interface shown in stereo. The interface is enlarged from the same direction as in (a). Amino acid residues involved in the dimerization are shown as stick models. The main chains of Asn24 and Ala222 are also shown as sticks. Hydrogen bonds are shown as yellow broken lines with their distances. (c) The overall structure of the native 4-pyridoxolactonase monomer. α-Helices, β-strands and loops are colored red, yellow and green, respectively. α-Helices (H1 - H13) and β-strands (S1 – S11) are numbered from the N-terminus. (d) The topology diagram of the monomer. The secondary structural elements are shown in the same manner as in (c). The numbers shown above and below of the elements correspond to the numbers of amino acid residue from the N-terminus.

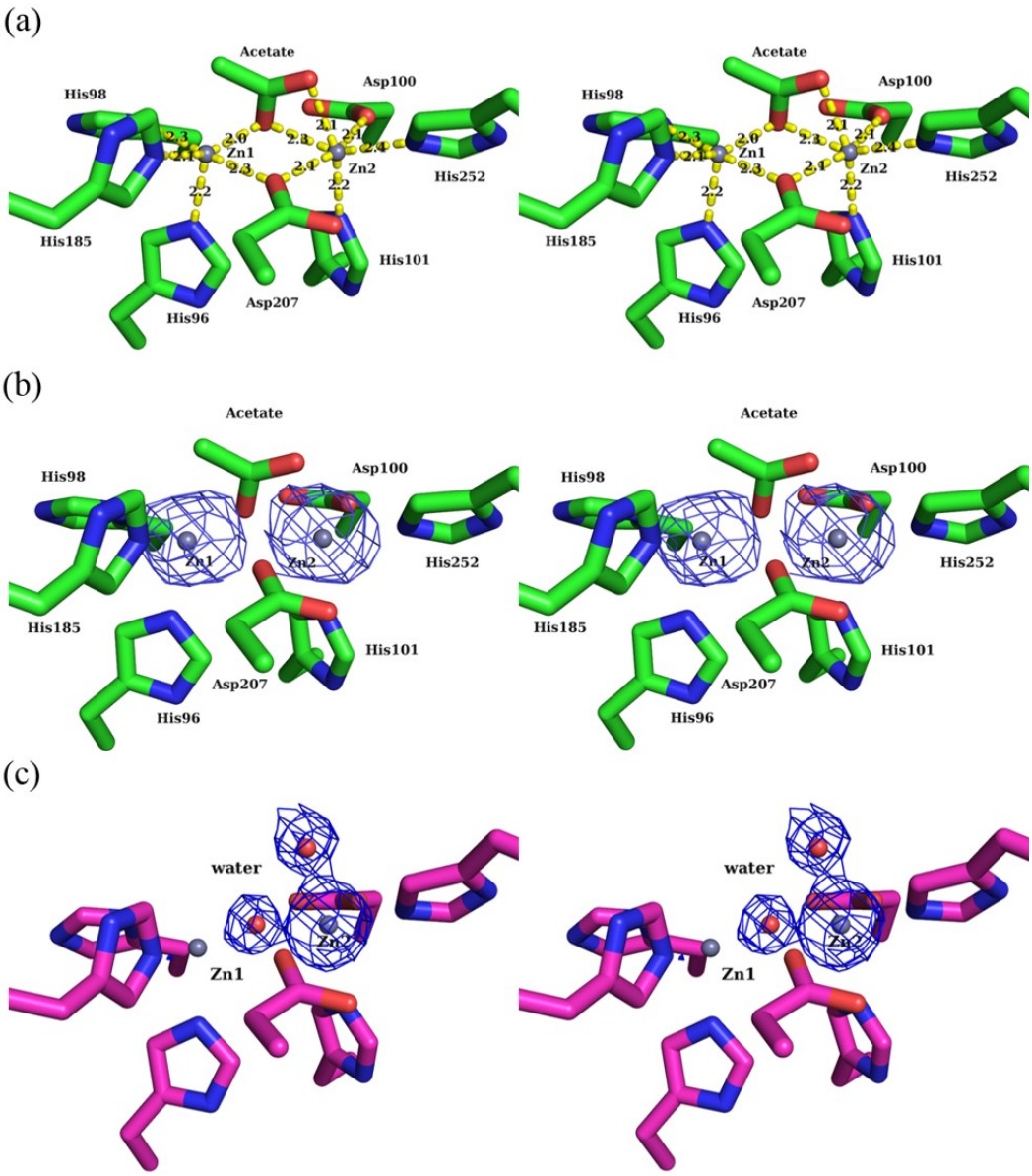

Figure 2. The active site of 4-pyridoxolactonase shown in stereo. (a) The active site of the native 4-pyridoxolactonase. Amino acid side chains are shown as green stick models. Zinc ions are shown as gray spheres. Coordination bonds are shown as yellow broken lines with their distances. (b) 2Fo-Fc maps around the zinc ions of the native 4-pyridoxolactonase contoured at 2.0 σ. (c) 2Fo-Fc maps around the zinc ions of the SeMet 4-pyridoxolactonase contoured at 2.0 σ.

5PAL complex

5PAL bound to two sites of the monomer (Fig. 3a). One 5PAL bound to the hydrophobic active site consisting of Leu14, Leu16, Phe33, Glu65, Phe99, Leu132, Gly133 and Phe223 (Fig. 3b). The pyridine nitrogen of 5PAL formed two hydrogen bonds with Oε1 and Oε2 of Glu65. The hydroxyl group at the C3 position formed a hydrogen bond with a catalytic water molecule that was the ligand of Zn1. The C3 hydroxyl group also formed a hydrogen bond with Oη of Tyr210. The carbonyl oxygen formed a hydrogen bond with N of Gly133. The lactone-ring formed π-stacking with Phe223. The other 5PAL bound to a part of protein surface formed by β-strands 1 and 2, α-helix 13 and the loop of 66-70 with a high B-factor (42.55, Fig. 3c). The pyridine nitrogen formed a hydrogen bond with Oγ of Ser13. The C3 hydroxyl group formed two hydrogen bonds with Oε2 of Glu70 and Oε1 of Gln73. The lactone oxygen and carbonyl oxygen formed hydrogen bonds with Nζ of Lys258. This binding of 5PAL on the surface may be an artifact of the crystal packing for two reasons: (i) 5PAL shows competitive but not allosteric inhibition, with only one binding site in the active site of 4-pyridoxolactonase (*1*). (ii) A part of this binding site, Arg32 in β-strand 2 and 67-68 loop region, was fixed by Gly166*-Asp168* region of an adjacent symmetrical molecule (not the crystallographic dimer), showing that crystal packing formed this binding site. The high B-factor of 5PAL also supports this consideration.

The hydrolytic reaction in the class B β-lactamases is initiated when the hydroxide ion nucleophically attacks the carbonyl carbon of a substrate (*2-5*). In the 4-pyridoxolactonase/5PAL complex, the carbonyl group of 5PAL pointed away from the candidate water molecule (5.8 Å between the carbonyl carbon and the water molecule), because the enzyme preferably recognized the C3 hydroxyl group of 5PAL over the

carbonyl oxygen. Thus, the lactone ring of 5PAL cannot be hydrolyzed but it can acts as the competitive inhibitor through the binding at the active site.

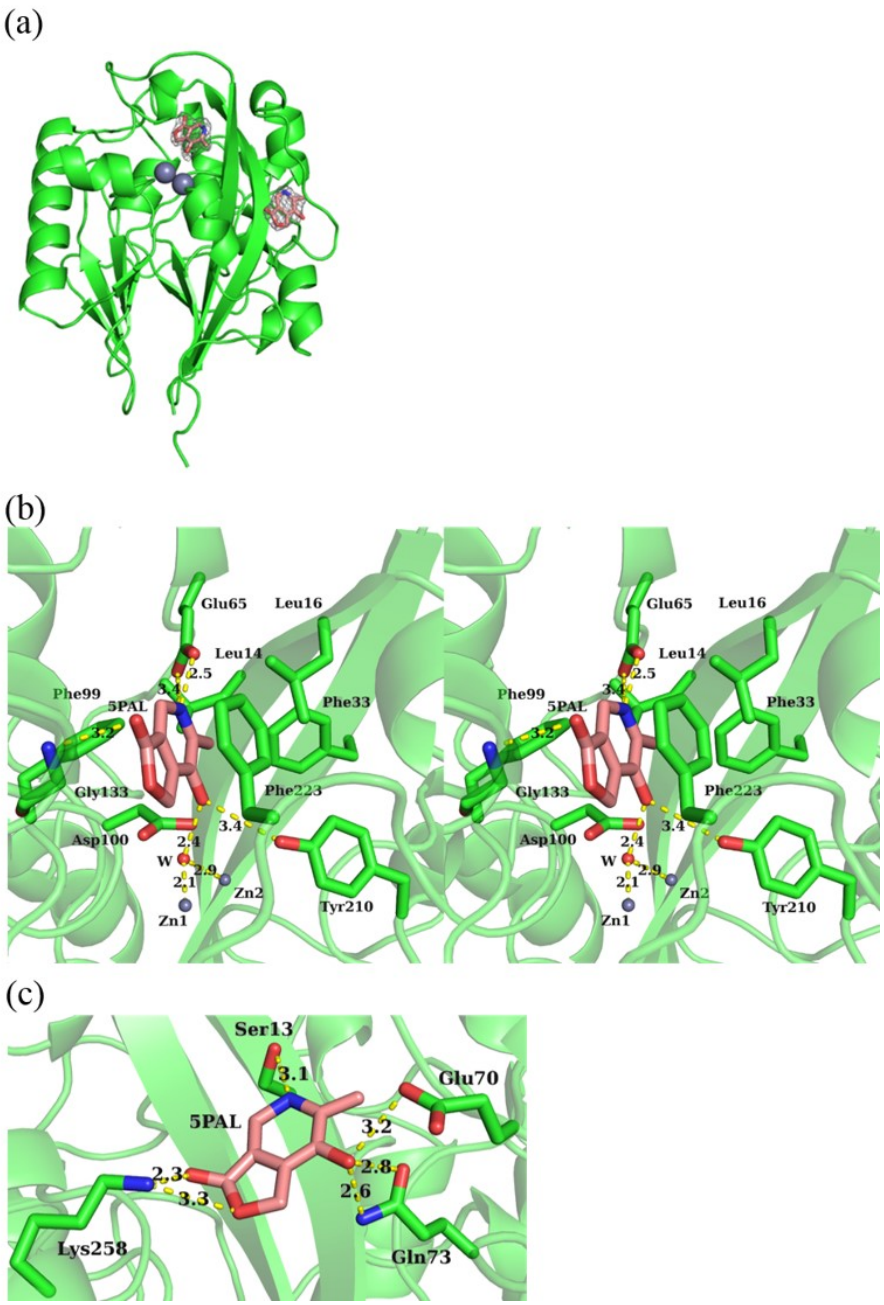

Figure 3. The binding modes of 5PAL. (a) Binding sites of 5PAL. 5PAL is shown as pink stick models. 2Fo-Fc maps of 5PAL are also shown as gray meshes, contoured at 1.0 σ. (b) The binding mode of 5PAL at the active site shown in stereo. The catalytic water molecule, which was located 5.8 Å apart from carbonyl carbon of 5PAL is shown above the Zn1 and Zn2 molecules. (c) The binding mode of 5PAL at the protein surface.

Docking simulation

The binding mode of 5PAL was compared with that of HSL in the AiiA/HSL complex (PDB ID: 2BR6) (*28*). The inhibitor HSL bound to AiiA through interactions with the two zinc ions as shown in Fig. 4a (between Zn1 and carbonyl oxygen and between Zn2 and lactone oxygen). When the substrate 4PAL is placed in the same position as HSL, the methyl group at the C2 postion makes a collision with the side chains of Glu65 and Phe99. This indicates that 4PAL interacts with the zinc ions in a different manner from the case of the AiiA/HSL complex. It also suggests that 4-pyridoxolactonase has a different catalytic mechanism from that of AiiA.

Determination of the structures of 4-pyridoxolactonase/4PAL and that/4PA complexes was not successful. Therefore, docking simulation of the structures were performed. A docking simulation of the structure of the 4-pyridoxolactonase/dianion intermediate (a reaction intermediate) complex was also performed. The best binding models were obtained based on the binding mode of 5PAL with binding energies, -5.15 for 4PAL, -15.29 for the dianion intermediate and -8.06 kcal/mol for 4PA, respectively. 4-Pyridoxolactonase showed the highest affinity towards the dianion intermediate.

4PAL bound to the similar position of 5PAL, and the carbonyl oxygen pointed towards the catalytic water (Fig. 4b). The pyridine nitrogen of 4PAL formed a hydrogen bond with Oε1 of Glu65 (2.8 Å). The C3 hydroxyl group formed two hydrogen bonds to the catalytic water (2.7 Å) and Oη of Tyr210 (2.7 Å). In contrast to the binding of 5PAL, the carbonyl oxygen of 4PAL interacted with Oη of Tyr210 (3.0 Å), Zn1 (2.7 Å) and the catalytic water (2.5 Å). The ring structure of the substrate formed a π-stacking with Phe223. The distance between the carbonyl carbon and the catalytic water (3.1 Å) was reasonable for nucleophilic attack of the water. Although an interaction between a

substrate and Zn2 which stabilizes the substrate binding and the subsequent intermediate formation has been observed in other subclass B3 enzymes (*4*, *29*), no interaction was observed between the substrate and Zn2 in 4-pyridoxolactonase. The simulated dianionic intermediate moved towards the zinc ions due to its negative charges (Fig. 4c). The C3 hydroxyl group formed a hydrogen bond with Oη of Tyr210 (2.6 Å) and became the ligand of Zn2 (1.8 Å). One of the deduced anionic oxygen interacted with Oδ1 of Asp100 (2.6 Å) and became the ligand of Zn1 (2.0 Å). The other anionic oxygen derived from the carbonyl oxygen of the substrate formed a hydrogen bond with Oη of Tyr210 (2.8 Å) and became the ligand of Zn1 (1.7 Å). The lactone oxygen weakly interacted with Zn1 (2.9 Å). In the simulated 4PA complex (Fig. 4d), the C3 hydroxyl group formed a hydrogen bond with Oη of Tyr210 (2.8 Å) and became the ligand of Zn2 (1.8 Å). The C4 carboxyl group also became the ligand of Zn1 (1.7 Å) and interacted with Oδ1 of Asp100 (2.7 Å). The carboxyl group occupied almost the same position as the catalytic water in the 4PAL complex (Fig. 4d).

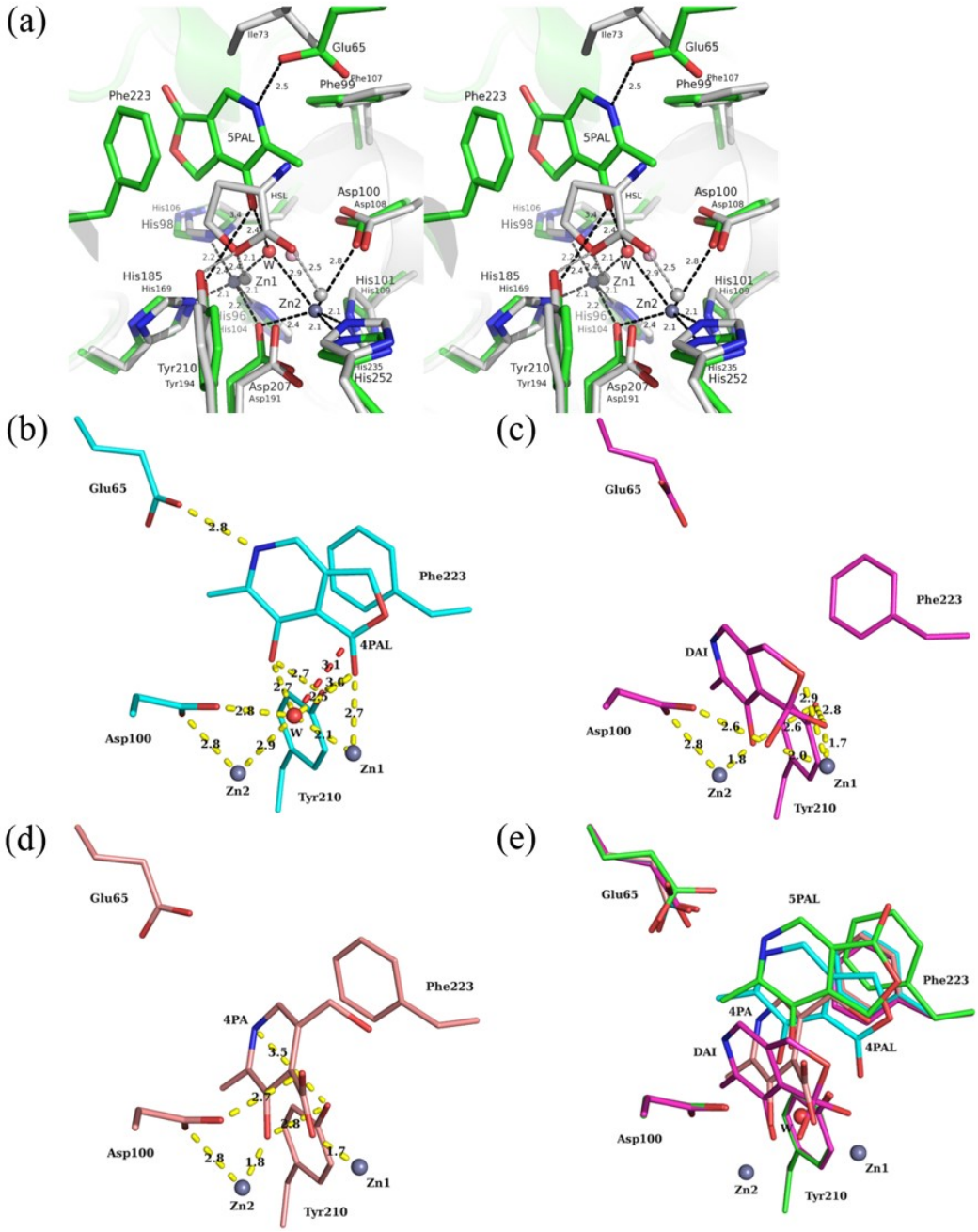

Figure 4. The comparison of the structures between the 4-pyridoxolactonase/5PAL and AiiA/HSL complexes, and the simulated binding modes of 4PAL, the dianion intermediate and 4PA in 4-pyridoxolactonase. (a) The comparison of the 4-pyridoxlactonase/5PAL (green) and AiiA/HSL (white) complexes shown in stereo. Interactions are shown as black broken line with their distances. (b) The simulated binding mode of 4PAL. Interactions are shown as yellow broken lines with the distances. The distance between the carbonyl carbon and the catalytic water is shown as a red broken line (3.1 Å). (c) The simulated binding mode of the dianion intermediate (DAI). (d) The simulated binding mode of 4PA. (e) Superimposition of all structures in 4-pyridoxolactnase. All models are superimposed to the 5PAL complex colored in green.

Catalytic mechanism

4-Pyridoxolactonase coordinated two zinc ions in the manner of the subclass B3 enzymes of the class B β-lactamase (Fig. 2). Therefore, it was assumed that the enzyme binds the substrate and catalyzes the reaction as in the subclass B3 enzymes. However, the simulated binding mode of the substrate was different from that of subclass B3 enzymes: no interaction was observed between the lactone oxygen of the substrate and Zn2. In this mode of binding, the anionic oxygen intermediate cannot be stabilized as discussed previously (*29*). The simulated binding modes of the substrate, intermediate and product give one possible catalytic mechanism (Scheme 2). The catalysis follows a subclass B2-like mechanism in which a dianion intermediate is formed (*5*). (i) 4PAL binds to the active site. The carbonyl oxygen of 4PAL interacts with Zn1 and forms a hydrogen bond with Oη of Tyr210. These interactions polarize the carbonyl group. Glu65 and Phe223 stabilize the proper substrate binding for initiation of the reaction. (ii) A catalytic water molecule between two zinc ions attacks the polarized carbonyl carbon to form a tetrahedral intermediate. Zn2 and Asp100 enhance the nucleophilicity of the water molecule. The O^- (from the carbonyl oxygen) of the tetrahedral intermediate coordinates to Zn1 by moving to the zinc ions. In accompaniment with this movement, the C3 hydroxyl group and the new hydroxyl group coordinate to Zn2 and Zn1, respectively. This movement also removes the interaction between the intermediate and Glu65 which neutralized the charge of the pyridine nitrogen. (iii) The dianion tetrahedral intermediate is then formed by transfer of a proton. The coordination of the C3 hydroxyl group with Zn2 weakens the interaction between Asp100 and Zn2, and makes the transfer of a proton between Asp100 and the new hydroxyl group easy (*29*). (iv) Finally, the product is formed and becomes the ligand of zinc ions. One cycle of the catalysis is completed by

dissociation of the product. A new water molecule occupies the vacated place for next catalytic cycle. The simulated binding energy of 4PA (-8.06 kcal/mol) is larger than that of 4PAL (-5.15 kcal/mol). This suggests that some conformational changes may occur during the formation and release of the product.

In this chapter, the author elucidated the crystal structure of 4-pyridoxolactonase and proposed the catalytic mechanism based on the docking simulation. The mechanism follows that found in subclass B2 enzymes and differs from that proposed in the AHL lactonases, AiiA (*29*) and AiiB (*25*), which catalyze the reaction following the mechanism of the subclass B3 enzymes. Although Asp100 in 4-pyridoxolactonase was conserved as Asp108 in AiiA and Asp115 in AiiB, respectively, Glu65 and Phe223 in 4-pyridoxolactonase were replaced by Ile73 and Gly207 in AiiA and Ala80 and Val230 in AiiB, respectively. There is no alternative functional group in AHL, such as the C3 hydroxyl group in 4PAL. These differences probably resulted in the difference of the catalytic mechanisms. 4-Pyridoxolactonase shows activity towards AHL, which is the substrate of AiiA and AiiB (*1*). The structure of the 4-pyridoxolactonase/AHL complex and the reaction mechanism of AHL catalyzed by 4-pyridoxolactonase will provide detailed information regarding the catalytic mechanism of class B β-lactamases. The author is continuing ~~our~~ study of this enzyme using X-ray crystallography, site-directed mutagenesis and kinetic analysis.

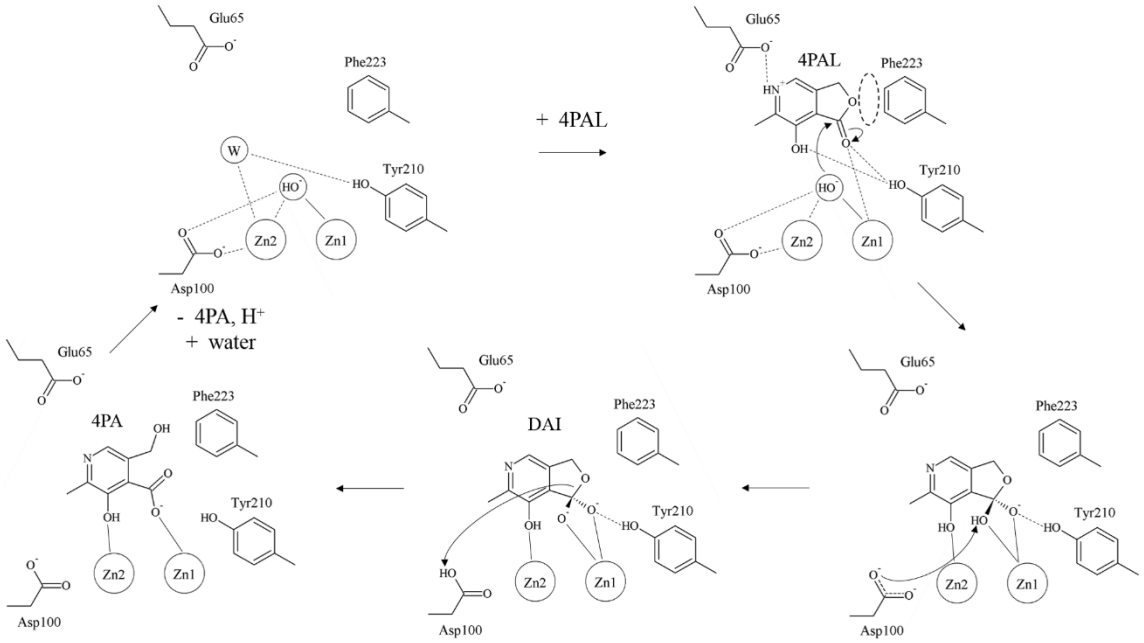

Scheme 2. A proposed catalytic mechanism of 4-pyridoxolactonase. Coordination bonds are shown as black lines. π-Stacking is shown as an ellipse (black broken line). Hydrogen bonds and interactions with zinc ions are shown as black broken lines.

References

1. Funami, J., Yoshikane, Y., Kobayashi, H., Yokochi, N., Yuan, B., Iwasaki, K., Ohnishi, K., and Yagi, T. (2005) *Biochim, Biophys, Acta.* **1753**, 234-239.
2. Wang, Z., Fast, W., Valentine, M., A., and Benkovic, J. S. (1999) *Curr. Opin. Chem. Biol.* **3**, 614-622.
3. Garau, G., Garcia-Sáez, I., Bebrone, C., Anne, C., Mercuri, P., Galleni, M., Frère, J-M., and Dideberg, O. (2004) *Antimicrob. Agents Chemother.* **48**, 2347-2349.
4. Palzkill, T. (2013) *Ann. N. Y. Acad. Sci.* **1277**, 91-104.
5. Bounaga, S., Laws, P. A., Galleni, M., and Page, I. P. (1998) *Biochem. J.* **331**, 703-711.
6. Matsuda, S., Yokochi, N., Yoshikane, Y., Kobayashi, J., Huy, C. N., Baba, S., Kuramitsu, S., Mikami, B., and Yagi, T. (2009) *Acta. Crystallogr.* F**65**, 886-889.

7. Mashida, S., Yu, Y., Singh, P. S., Kim. J-D., Hayashi, K., and Kawata, Y. (1998) Overproduction of β-glucosidase in active form by an *Escherichia coli* system coexpressing the chaperonin GroEL/ES, *FEMS Microbiol. Lett.* **159**, 41-46.
8. Otwinowski, Z., and Minor, W. (1997) *Methods Enzymol.* **276**, 307-326
9. Sheldrick, M. G. (2010) *Acta. Crystallogr.* D**66,** 479-485.
10. Terwilliger, T. C., and Berendzen, J. (2000) *Acta. Crystallogr.* D**56**, 965-972.
11. Terwilliger, T. C. (2003) *Acta. Crystallogr. D***59**, 38-44.
12. Afonine, P. V., Grosse-Kunstleve, R. W., Echols, N., Headd, J. J., Moriarty, N. W., Mustyakimov, M., Terwilliger, T. C., Urzhumtsev, A., Zwart, P. H., and Adams, P. D. (2012) *Acta. Crystallogr.* D**68**, 352-367.
13. Emsley, P., Lohkamp, B., Scott, G. W., and Cowtan, K. (2010) *Acta. Crystallogr.* D**66**, 486-501.
14. Vagin, A., and Teplyakov, A. (1997) *J. Appl. Cryst.* **30**, 1022-1025.
15. Winn, D. M., Ballard, C. C., Cowtan, D. K., Dodson, J. E., Emsley, P., Evans, R. P., Keegan, M. R., Krissinel, B. E., Lesile, W. G. A., McCoy, A., McNicholas, J. S., Murshudov, N. G., Pannu, S. N., Potterton, A. E., Powell, R. H., Read, J. R., Vagin, A., and Wilson, S. K. (2011) *Acta. Crystallogr*. *D***67**, 235-242.
16. Murshudov, N. G., Vagin, A. A., and Dodson, J. E. (1996) *Acta. Crystallogr.* D**53**, 240-255.
17. Schuttelkopf, W. A., and Aalten van, F. M. D. (2004) *Acta. Crystallogr.* D**60**, 1355-1363.
18. Laskowski, R. A., MacArthur, M. W., Moss, D. S., and Thomton, J. M. (1993) *J. App. Cryst.* **26**, 283-291.
19. Vaguine, A. A., Richelle, J., and Wodak, S. J. (1999) *Acta. Crystallogr.* D**55**, 191-

205.

20. Holm, L., and Rosenström, P. (2010) *Nucl. Acids Res.* **38**, 545-549.
21. Krissinel, E., and Henrick, K. (2007) *J. Mol. Biol.* **372**, 774-797.
22. Morris, G. M., Huey, R., Lindstrom, W., Sanner, M. F., Belew, R. K., Goodsell, D. S., and Olson, A. J. (2009) *J. Comput. Chem.* **30**, 2785-2791.
23. Ramachandran, G. N., and Sasisekharan, V. (1968) *Adv. Protein. Chem.* **23**, 283-438.
24. Jones, S., and Thornton, J. M. (1996). *Ploc. Natl. Acad. Sci. U.S.A.* **93**, 13-20.
25. Liu, D., Thomas, P. W., Momb, J., Hoang, Q. Q., Petsuko, G. A., Ringe, D., and Fast, W. (2007) *Biochemistry* **46**, 11789-11799.
26. Liu, D., Momb, J., Thomas, P. W., Moulin, A., Petsuko, G. A., Fast, W., and Ringe, D. (2008) *Biochemistry* **47**, 7706-7714.
27. Auld, D. S. (2001) *Biometals* **14**, 271-273.
28. Kim, M. H., Choi, W. C., Kang, H. O., Lee, J. S., Kang, B. S., Kim, K.-J., Derewends, Z. S., Oh, T.-K., Lee, C. H., and Lee, J. K. (2005). *Ploc. Natl. Acad. Sci. U.S.A.* **102**, 17606-17611.
29. Momb, J., Wang, C., Thomas, P. W., Petsko, G. A., Guo, H., Ringe, D., and Fast, W. (2008) *Biochemistry* **47**, 7715-7725.

Chapter 2

Role of Tyr270 in 2-Methyl-3-hydroxypyridine-5-carboxylic Acid Oxygenase

Introduction

2-Methyl-3-hydroxypyridine-5-carboxylic acid oxygenase (MHPCO) catalyzes the FAD-dependent pyridine-ring opening reaction of MHPC to AAMS (*1*). This reaction adds two oxygen atoms to MHPC and then cleaves the pyridine-ring in the presence of FAD, NADH, molecular oxygen and water. This activity is divided into three reactions (*2*): (i) a binding of a substrate and a hydride transfer between FAD and NADH (reductive-half reaction), (ii) a hydroxylation of the substrate (oxidative-half reaction) and (iii) a further oxygenation and ring-opening of the substrate (ring-opening reaction). MHPCO also shows basal NADH oxidation activity uncoupled ring-opening in the absence of the substrate (MHPC) as found in other NAD(P)H-dependent flavoenzymes (*1*). The mechanism is: (i) reduction of FAD by NAD(P)H to form $FADH_2$ (reductive-half reaction) and (ii) reduction of a molecular oxygen to form H_2O_2 (oxidative-half reaction). Although both ring-opening and basal activities occur via similar reduction pathway, the reduction rate in the ring-opening activity only is enhanced to several-thousands-fold. This phenomenon is said to “effector role of substrate” (*2*). The crystal structures of SeMet MHPCO and its MHPC complex were recently determined and the catalytic mechanisms of the oxidative-half and ring-opening reactions in the presence of MHPC

have been discussed (*2*, *3*). However, the mechanisms of the reductive-half reactions based on the crystal structure have not been discussed.

MHPCO shows the ring-opening activity not only toward MHPC, but also toward 5-hydroxynicotinic acid (5HN) and 5PA (*1*, *4*, *5*), which have a 3-hydroxypyridine-5-carboxylic acid backbone (Scheme 1). The enzyme has similar affinities for the three compounds: the K_m values for MHPC, 5HN and 5PA are 25, 60 and 50 μM, respectively. Although the enzyme shows the same activity toward MHPC and 5HN, it shows extremely low activity toward 5PA (5% of activities toward MHPC or 5HN).

In this chapter, I describe that Tyr270 is essential for "effector role of substrate" (the reductive-half reaction) based on the crystal structures of MHPCO and its 5PA complex and kinetic analyses of the WT enzyme, Y270F and Y270A mutants.

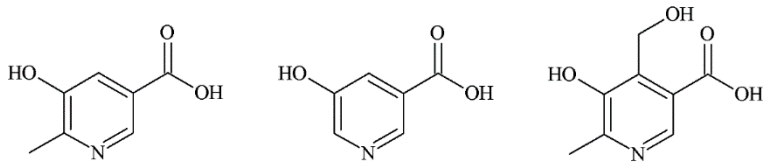

Scheme 1. Substrates of MHPCO.

Materials and Methods

Bacterial strain, plasmid and reagents

A bacterial strain, plasmid and reagents reported previously were used (*5*). The plasmid vectors of the Y270F and Y270A mutants were prepared from that of the WT enzyme using a KOD -Plus- Mutagenesis Kit (TOYOBO) according to the instruction manual. The primers for the Y270F mutant were 5'- TTCGAAACGACCAAGCTGGAT

AGC-3' and 5'-CTTGTCGTACCTGGCGGTTTTAAGC-3'. The primers for the Y270A mutant were 5'-GCCGAAACGACCAAGCTGGATAGC-3' and 5'-CTTGTCGTACCT GGCGGTTTTAAGC-3'. 5HN was purchased from Tokyo Chemical Industry. The concentration of 5HN was calculated from a molecular absorption coefficient (ε = 4.19 mM^{-1} cm^{-1}) at 315 nm in 0.1 N NaOH (*6*). 5PA was prepared from alkaline-hydrolysis of 5PAL using NaOH. After neutralization by HCl, the yield was checked by reversed-phase isocratic high-performance liquid chromatography (HPLC) (*7*). 5PA was obtained in a yield of 70%. NADH and NAD^+ were purchased from Oriental Yeast.

Expression

The method used to induce the expression of the WT enzyme was described previously (*5*). But the culture volume was set at 400 ml, and 0.25% (w/v) lactose (final concentration) was added to the LB medium. The culture time was set at 48 hr. The expression method for the mutants was the same as that for the WT enzyme.

Purification

The WT enzyme was purified as reported previously (*5*), with some modifications. The recombinant *E. coli* BL21(DE3) cells (5.75 g) were suspended in 50 ml of sonication buffer [100 mM sodium phosphate buffer (SPB) (pH 8.0), 14 mM 2ME, 5 mM ethylenediaminetetraacetic acid (EDTA) and 0.1 mM phenylmethylsulfonyl-fluoride (PMSF)]. The suspension was sonicated for 1 min using a SONIFIER 250 (Branson Ultrasonics) and cooled for 5 min on ice. This process was repeated five times. A crude extract was obtained by centrifugation at 8,000 g for 30 min at 4°C. Ammonium sulfate powder was added to the crude extract to a 40% saturated concentration with weak

stirring and cooling on ice. After 1 hr on ice, a yellow precipitate was obtained by centrifugation at 8,000 g for 30 min at 4ºC. The yellow precipitate was dissolved in Buffer A [20 mM SPB (pH 8.0), 14 mM 2ME, 0.3 mM EDTA] and thoroughly dialyzed against the same buffer while the conductivity was checked using an ES-12 conductivity meter (HORIBA). After the dialysis, the sample was filtered with a MILLEX®-HV filter (0.45 μm) (Millipore) and then applied to a HiLoad™ 26/10 Q-Sepharose™ High Performance column connected to an AKTAprime plus system (GE Healthcare Bioscience). The column was equilibrated with Buffer A and then the sample was applied. The column was washed with 100 ml of Buffer A, and then the proteins bound to the column were eluted by a linear gradient with Buffer A supplemented with 0.5 M NaCl. Fractions with both the FAD-originated yellow color and ring-opening activity were eluted at around 0.3 M NaCl. The fractions were checked by SDS-PAGE, collected and concentrated by 0-45% saturated ammonium sulfate precipitation. After centrifugation, solubilization and dialysis with and against Buffer A, the sample was filtered and applied to a MonoQ HR 16/10 column (GE Healthcare) equipped with an LC-10Ai HPLC pump system (Shimadzu). The column was equilibrated with Buffer A and then the sample was applied. The column was washed with 40 ml of Buffer A, and then proteins bound to the column were eluted by a linear gradient with Buffer A supplemented with 0.5 M NaCl. Yellow fractions exhibiting the ring-opening activity were eluted around 0.2 M NaCl. The fractions were checked by SDS-PAGE, then collected and activated by FAD and 2ME, because MHPCO reversibly inactivates at 4ºC (*6*). 0.5 mM FAD and 50 mM 2ME were added to the sample and then incubated at 25ºC for 30 min. After the activation, the excessive FAD and 2ME were removed by a dialysis against Buffer A. After the dialysis, the sample was used for all experiments. The protein concentration was measured by a

Bio-Rad Protein Assay (Bio-Rad) using bovine serum albumin as a standard. The concentration of the purified enzyme was determined from the molecular absorption coefficient (ε = 329,012 M^{-1} cm^{-1}) at 280 nm (*5*). The mutants were also purified by the same procedure.

Crystallization and structure analysis

After the activation and dialysis, the enzyme solution of the WT enzyme was ultra-filtered to 10 mg/ml by a VIVASPIN 20 (10,000 MWCO, Sartorius Stedim Biotech). The solution was applied to screening with Crystal Screen I and II (Hampton Research) and Wizard I and II (Emerald Biosystems) by the sitting-drop vapor-diffusion method at 4^{o}C and 20^{o}C. After optimization, the best crystals of the WT enzyme were obtained by mixing 1 μl of the enzyme and 1 μl of the reservoir solution [8% PEG8,000, 0.1 M Tris-HCl (pH 8.5)] using the hanging drop method at 20^{o}C for 2 weeks. Crystals of the WT/5PA complex were also prepared under the same condition, except that 1 mM 5PA (final concentration) was added to the enzyme solution.

The crystals of the WT enzyme and its 5PA complex were picked up from droplets and flash-cooled by a nitrogen-gas stream at -173^{o}C after quick soaking in a reservoir solution containing 30% (v/v) glycerol. Diffraction data of the crystals were collected by synchrotron radiation with wavelength 1.0 Å at PF-AR NW12A of KEK. Both data sets were processed using HKL2000 (*8*). The phases were determined by a molecular replacement program, MOLREP (*9*) in CCP4 (*10*), with SeMet MHPCO (PDB code 3GMB chain A) as a template (*3*). Both structures were refined by REFMAC5 (*11*) and PHENIX (*12*). Refinement by PHENIX and modeling by COOT (*13*) were repeated until interpretable difference-Fourier maps were completed. Water molecules were added

by COOT. The model of 5PA was generated from PRODRG (*14*). After the refinement, the final models were evaluated by PROCHECK (*15*) and SFCHECK (*16*). The data collection and refinement statistics are shown in Table I. The oligomer structure of MHPCO was analyzed by PISA (*17*). The coordinates and structure factors have been deposited in the PDB under the accession numbers 4JY2 (the WT enzyme) and 4JY3 (the WT/5PA complex).

Table I. Data collection and refinement statistics.

	WT (4JY2)	WT + 5PA (4JY3)
Data collection		
X-ray source	PF-AR NW12A	
Wavelength (Å)	1.0000	
Crystal system	monoclinic	Monoclinic
Space group	*C2*	*C*2
Unit cell parameter (Å,°)	*a* = 110.738, *b* = 129.364, *c* = 89.302, *β* = 122.51,	*a* = 111.446, *b* = 129.526, *c* = 89.565, *β* = 122.70
Resolution limit (Å)	50 - 1.94 (2.01-1.94)	50 - 1.77 (1.83-1.77)
Measured reflections	299594 (29560)	364258 (30578)
Unique reflections	78611 (7779)	103436 (9864)
Redundancy	3.8 (3.8)	3.5 (3.1)
Completeness (%)	100 (100)	99.5 (95.6)
$< I/\sigma(I) >$	7.5 (4.1)	8.6 (3.5)
R_{merge} (%)	9.9 (30.8)	8.2 (31.5)
Refinement		
Resolution range (Å)	49.07-1.94 (1.96-1.94)	41.82-1.77 (1.79-1.77)
R-factor (%)	16.8 (19.6)	15.6 (20.6)
R_{free} (%)	20.1 (24.4)	17.9 (24.1)
Overall B value (Å^2)	14.81	14.02
Amino acid residue	370 × 2	370 × 2
FAD	2	2
5PA	-	2
Water	637	931

Values in parentheses are for the highest resolution shell.

Analysis of the enzyme reaction by HPLC

A reaction mixture (250 μl) consisting of 50 mM SPB (pH 8.0), 10 mM 2ME, 0.3 mM NADH and 0.2 mM 5HN was pre-incubated for 5 min at 25ºC. Then, the reaction

was initiated by the addition of the WT enzyme (0.36 μM) or Y270F mutant (3.6 μM), respectively. After 1, 5 or 30 min, 20 μl of 6 N HCl was added to terminate the reaction. The acidic sample was ultra-filtered by a VIVASPIN 500 (10,000 MWCO) at 19,000 g at 4ºC for 1 min. The substrates (5HN and NADH) and reaction product (NAD^+) in the filtrate (20 μl) were quantified at 20ºC by reversed-phase isocratic HPLC on a 5C18-AR-300 column (Nacalai Tesque) at a flow rate of 0.5 ml/min. The amount of α-(*N*-formylaminomethylene) succinic acid (FAMS) was calculated from the peak area based on the amount of 5HN. All substrates and products were detected by the absorption at 285 nm. The mobile phase consisted of 20 mM H_3PO_4 and 0.5% (w/v) acetonitrile.

Steady-state kinetics

Commercially available 5HN was used as a substrate in the enzyme reactions with the WT enzyme and the mutants, because MHPCO shows almost same activity toward 5HN as MHPC (*1*, *2*). 5PA was not used as a substrate because the mutants showed undetectable activity toward it. The ring-opening activity was determined in a reaction mixture (total volume 1 ml) consisting of 50 mM SPB (pH 8.0), 10 mM 2ME, 0.3 mM NADH and 0.2 mM 5HN at 25ºC. 2ME could be replaced with 1 mM DTT. In the assay of the Y270F mutant, the 5HN concentration was changed to 7 mM. The produced FAMS was determined by HPLC described above. One unit (U) of the enzyme was defined as the amount of the enzyme that catalyzed the ring-opening reaction of 1 μmol of FAMS per minute. The concentrations of the WT enzyme and the Y270F and Y270A mutants were set at 0.09, 0.9 and 3 μM, respectively. The NADH oxidation activity uncoupled with ring-opening was measured in the absence of 5HN in the reaction mixture described above. The oxidation of NADH was measured based on the decrease in absorbance at 366

nm (ε = 3.21 mM^{-1} cm^{-1}). The concentrations of the WT enzyme and the Y270F and Y270A mutants were set at 6.0, 0.9 and 0.9 μM, respectively. All kinetic parameters were calculated by using KaleidaGraph software.

K_m and V_{max} were calculated from Michaelis-Menten kinetics (eq. 1).

$V_0 = V_{max}$ [S] / (K_m + [S]) (eq. 1)

K_m, K_i and V_{max} were calculated from substrate inhibition kinetics (eq. 2).

$V_0 = V_{max}$ [S] / (K_m + ([S] (1 + [S] / K_i))) (eq. 2)

k_0 was calculated by equation 3 (eq. 3).

$k_0 = V_{max}$ / [E] (eq.3)

Because MHPCO is a homotetrameric enzyme, k_{cat} was calculated by equation 4 (eq.4).

$k_{cat} = k_0$ / 4 (eq.4)

Results and Discussion

Purification

The WT enzyme and the mutants were expressed in *E. coli*. The expression levels of the WT enzyme and the mutants were almost the same (~16% in the crude extracts using SDS-PAGE densitogram). They were purified to homogeneity by ammonium sulfate fractionation, Q-Sepharose and Mono Q column chromatography. After the activation with 0.5 mM FAD and 50 mM 2ME, the WT enzyme showed a higher specific activity in the ring-opening activity (2.98 U/mg) than that reported previously (~2.8 U/mg) (*5*). The specific activities of the Y270F and Y270A mutants were significantly lower (0.399 U/mg for the Y270F mutant; 0.00929 U/mg for the Y270A mutant). The activities of all purified enzymes were maintained for 2 weeks in Buffer A. The mutations did not affect the expression level or protein stability, but significantly decreased the ring-

opening activity.

Crystal structure determined

The initial phases of the WT enzyme and its 5PA complex were determined by the molecular replacement method, and then both structures were refined as shown in Table I. Ramachandran plots (*18*) of the WT enzyme and its 5PA complex by PROCHECK (*15*) showed that 91.7% and 91.9% of the amino acid residues existed in the most favored region, 7.8% and 7.8% in the additionally allowed region, 0.2% and 0% in the generously allowed region and 0.3% and 0.3% in the disallowed region, respectively.

Tetrameric structure of MHPCO

In the crystal structures of the WT enzyme and its 5PA complex, two monomers existed in the asymmetric unit (Fig. 1, chains A and B), although the enzyme exists as a tetramer in solution (*5*). The monomers of the dimer interacted with their Met86-Lys89 and Phe205-Trp206 residues, respectively. This dimer forms a tetramer with two symmetrical monomers related by a two-fold axis (Fig. 1, chains A* and B*). In the tetramer, chains A and A* (chains B and B*) formed two intermolecular hydrogen bonds between O of Asn97 and Nη1 of Arg102* and between Nη1 of Arg102 and O of Asn97*), four salt bridges less than 3.8 Å (between Arg61 and Glu64*, between Glu64 and Arg61*, between Asp70 and Arg372*, and between Arg372 and Asp70*) and C-C contacts between the side chains of Leu73 and Trp377* and between Trp377 and Leu73*. Furthermore, two ring-stacking interactions existed between His193 of chain A and that of chain B* (or between chains B and A*). The buried solvent-accessible surface area per

monomer by this tetramerization was ~1200 Å^2 (~7.8% of the whole area) by PISA (*17*). This tetramer may represent a functional tetramer in solution phase.

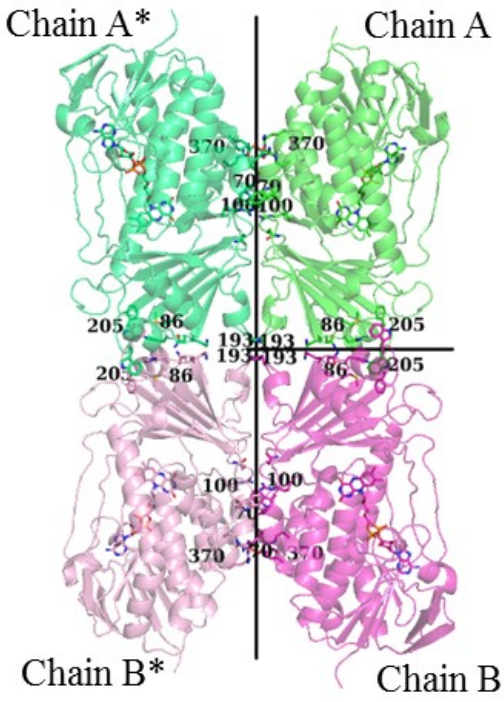

Figure 1. Possible tetrameric structure. Chains A and B in an asymmetrical unit are colored green and magenta, respectively. The chains are related by a two-fold axis (short black line). One possible tetramer is formed by symmetrical molecules (A* and B*) that are related by a two-fold axis (long black line). The residues involved in the dimer and the tetramer interfaces are labeled. FAD is shown as stick models.

Structure of the WT enzyme

The monomers (chains A and B) showed little structural difference (RMSD = 0.052 Å for 2366 atoms). The 1-9 N-terminal residues of the monomers could not be assigned due to their disorder. The overall structure of the monomer consisted of an FAD-binding domain (10-80, 95-178 and 268-379 residues) and a substrate-binding domain (81-94 and 179-267 residues) formed by an α/β fold (Fig. 2). An active site existed in a cleft between the domains. The structures of the WT enzyme and the reported SeMet

enzyme (*3*) were quite similar (each chain A, RMSD = 0.147 Å for 2442 atoms, Fig. 2). However, Cys294 of the WT enzyme formed a mixed disulfide bond with 2ME, in which Oζ did not make any hydrogen bond with the adjacent amino acid residue.

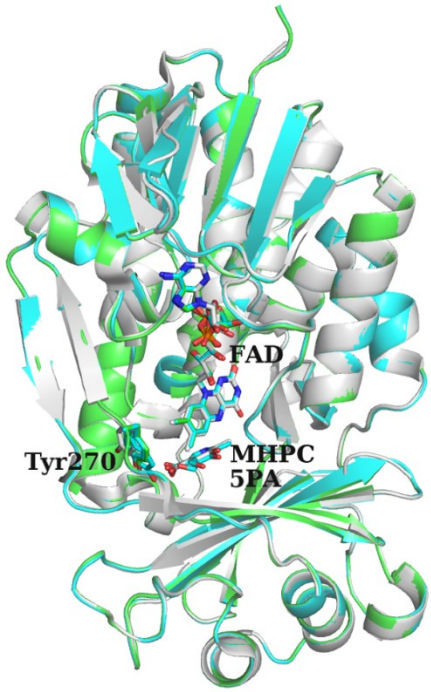

Figure 2. Comparison of the monomers (chain A) of the WT enzyme and WT/5PA complex, and the SeMet/MHPC complex. The WT enzyme, WT/5PA complex and the SeMet/MHPC complex are shown in green, cyan and gray, respectively. FAD, MHPC, 5PA and Tyr270 are shown as stick model. 5PA and MHPC occupy the same position.

Structure of the WT/5PA complex

The monomers (chains A and B) in the asymmetrical unit of the WT/5PA complex were almost the same (RMSD = 0.052 Å for 2373 atoms). The overall structures of the WT enzyme and WT/5PA complex were also quite similar (each chain A, RMSD = 0.060 Å for 2515 atoms, Fig. 2). However, significant local differences were observed in three parts: the Trp173-Asp177 and Lys269-Glu271 residues in the WT/5PA complex moved to a solvent side (~1 Å) and to the active site (~1 Å), respectively. The side chain of Tyr270 in the WT/5PA complex took two conformations (A and B) with the same

occupancies (Fig. 3). In conformation A, it moved to the active site (~3 Å) to interact with the bound 5PA. In conformation B, the position of Tyr270 was the same as that of the WT enzyme.

5PA also bound to the active site in two conformations, and the occupancies were 0.37 and 0.34 in conformations A and B, respectively (Fig. 4). In two conformations, the N1 atom of 5PA formed one possible hydrogen bond with O of Pro295, and two water-mediated hydrogen bonds with Oη of Tyr82 and O of Ala296. The hydroxyl group at the C3 position formed three water-mediated hydrogen bonds with the O4 and N5 atoms of the isoalloxazine ring of FAD and Oη of Tyr223. It also formed a water-mediated hydrogen bond with the Oη of Tyr223 through another water molecule. The carboxyl group at the C5 position formed a hydrogen bond with Nε of Arg211 and a water-mediated hydrogen bond with N of Ala296. In contrast, the positions of the hydroxymethyl group at the C4 position were different between the two conformations. One hydroxymethyl group at the C4 position in conformation A formed water-mediated hydrogen bonds with Oη of Tyr223. On the other hand, that in conformation B formed direct or water-mediated hydrogen bonds with Tyr270 in conformation A or B, respectively.

Thus, the binding of 5PA led to the conformational change of Tyr270 by the hydroxymethyl group at the C4 position. From the activity differences among MHPC, 5HN and 5PA (*1*, *2*, *4*, *5*) and the crystal structure of the SeMet MHPCO/MHPC complex (Fig. 3, right) (*3*), this conformational change probably led to the activity decrease by 5PA.

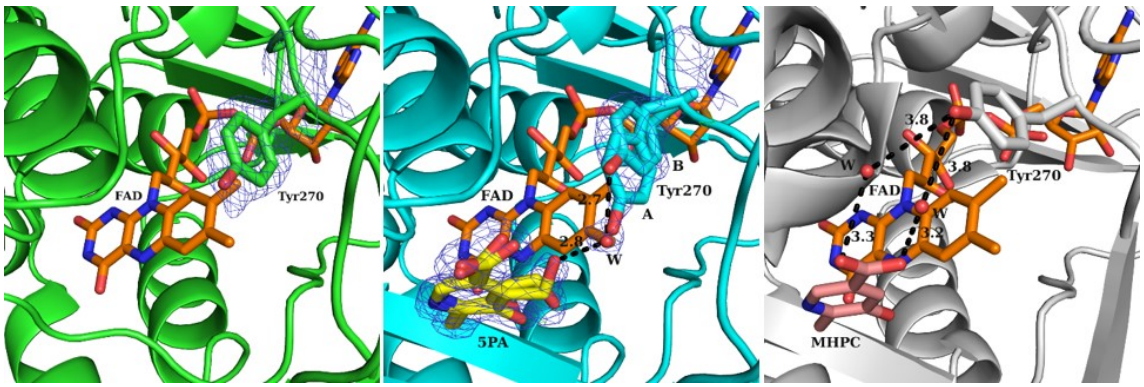

Figure 3. Conformational change of Tyr270 in the absence (left, green) and presence (center, cyan) of 5PA. The structure of SeMet/MHPC complex (right, gray) is also shown for comparison. FAD, 5PA and MHPC are colored orange, yellow and pink, respectively. Water molecules are shown as red spheres. Hydrogen bonds are shown as black broken lines with their distances. 2Fo-Fc maps are shown in blue meshes contoured at 1.0 σ. Fo-Fc maps are shown in green (positive) and red (negative) meshes contoured at 3.5 σ, respectively.

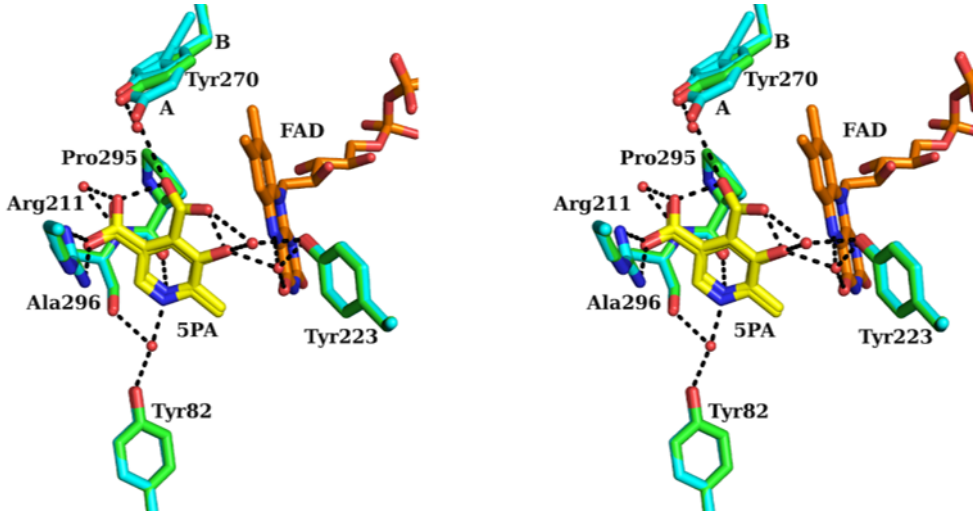

Figure 4. The binding mode of 5PA shown in stereo. The structure of the WT enzyme (green stick model) is superimposed on the WT/5PA complex (cyan stick model). The FAD of the WT enzyme is completely superimposed.

Analysis of the enzyme reaction by HPLC

The decrease of substrates and the increase of products of the WT enzyme and the Y270F mutant were determined by HPLC (Fig. 5). NADH, 5HN, FAMS and NAD^+ were eluted at 9.3, 9.7, 13.8 and 16.6 min, respectively. The peak at 13.8 min was

considered to represent FAMS because its retention time was similar to that of succinic acid. Both enzymes consumed and produced almost equimolar amounts of the substrates and products at 1 and 5 min, but the activity of the Y270F mutant was 5% of the activity of the WT enzyme. The WT enzyme changed all of 5HN into FAMS at 30 min. In contrast, the Y270F mutant could not change 50% of 5HN into FAMS, because 50% of NADH was changed to NAD^+ to form H_2O_2 without coupling to the ring-opening reaction. Thus, the Y270F mutant had a high basal NADH oxidation activity.

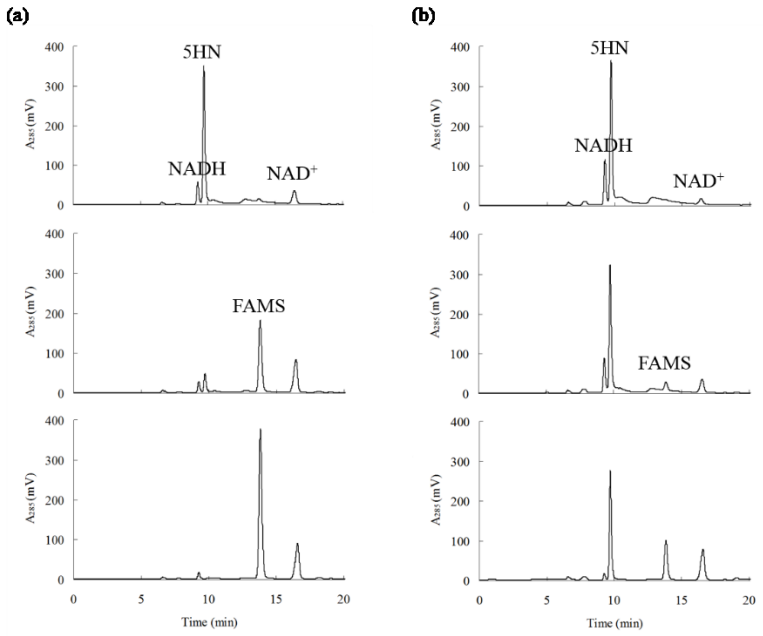

Figure 5. HPLC elution patterns of the substrates and products in the reaction mixtures with the WT enzyme and the Y270F mutant. (a) Reaction with the WT enzyme. (b) Reaction with the Y270F mutant. Elution patterns of the reaction mixtures stopped at 1, 5 and 30 min are shown in the top, middle and bottom panels, respectively.

Steady-state kinetics

The effect of 5HN concentration on the ring-opening activity of the WT enzyme and the Tyr270 mutants were examined (Fig. 6 and Table II). The ring-opening activity of the WT enzyme was inhibited at a high concentration of 5HN (R = 0.998, K_i = 480 μM, Fig. 6a). The Y270F and Y270A mutants showed a low but measurable ring-opening activity toward 5HN. The activities were not inhibited at the high concentration of 5HN (Fig. 6a).

Table II. Summary of kinetic parameters.

	Ring-opening activity					NADH oxidation activity		
	$K_{m\ 5HN}$	$K_{i\ 5HN}$	$K_{m\ NADH}$	k_{cat}	k_{cat} / K_m	$K_{m\ NADH}$	k_{cat}	k_{cat} / K_m
	(μM)	(μM)	(μM)	(s^{-1})	($M^{-1}s^{-1}$)	(μM)	(s^{-1})	($M^{-1}s^{-1}$)
WT	60 ± 6	480 ± 50	100 ± 6	$1.3 \times 10^3 \pm 50$	2.2×10^7	1200 ± 100	0.19 ± 0.01	1.6×10^2
Y270F	210 ± 50	-	120 ± 10	19 ± 1	9.1×10^4	310 ± 20	7.4 ± 0.2	2.4×10^4
Y270A	45 ± 20	-	470 ± 40	0.050 ± 0.003	1.1×10^3	530 ± 40	0.84 ± 0.05	1.6×10^3

The WT enzyme showed a 6800-fold higher turnover number of the ring-opening activity than that of the NADH oxidation activity uncoupled with ring-opening (1300 and 0.19 s^{-1}, respectively). The Y270F mutant showed much lower ring-opening activity and its ring-opening activity became similar level of the NADH oxidation activity uncoupled with ring-opening (19 and 7.4 s^{-1}, respectively). Furthermore, the Y270A mutant showed the slightly higher NADH oxidation activity uncoupled with ring-opening than the ring-opening activity (0.05 and 0.84 s^{-1}, respectively). Thus, Tyr270 is essential for enhancing the ring-opening activity. In contrast to the turnover numbers, the WT enzyme and the mutants showed similar K_m values for 5HN (60, 210 and 45 μM, respectively) and for NADH (100, 120 and 470 μM, respectively) in the ring-opening activity. The K_m values for NADH in the NADH oxidation activity uncoupled with ring-opening were also similar among them: 1200, 310 and 530 μM for the WT enzyme, and the Y270F and Y270A mutants, respectively. The results showed that Tyr270 is significantly involved in the ring-opening activity but not in the binding of the substrates.

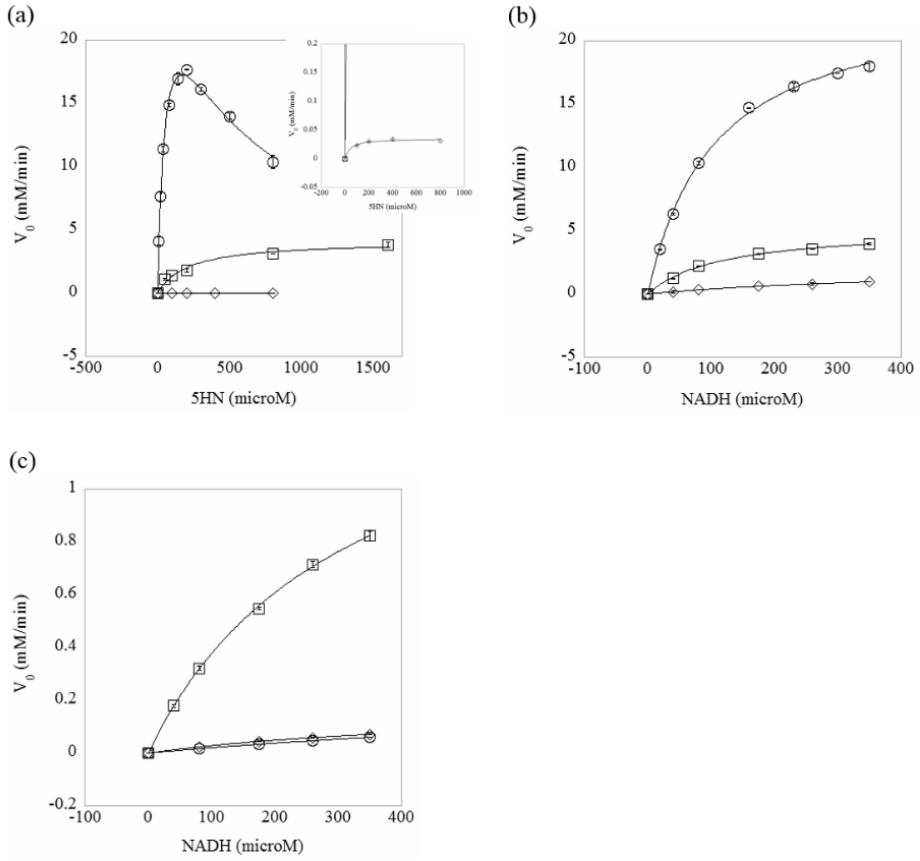

Figure 6. Effects of substrate concentrations on the ring-opening activity and NADH oxidation activity uncoupled with ring-opening. The activities of the WT enzyme and the Y270F and Y270A mutants are indicated with circles, squares and diamonds, respectively. (a) Effect of 5HN concentration in the ring-opening activity. The activity of the Y270A mutant is enlarged in the inset. (b) Effect of NADH concentration in the ring-opening activity. (c) Effect of NADH concentration in the NADH oxidation activity uncoupled with ring-opening. The average and standard deviation of two to four independent measurements are shown.

Role of Tyr270 in the MHPCO reaction

From the crystal structures of the WT MHPCO and its 5PA complex, Tyr270 was considered to be involved in the reaction. The site-directed mutagenesis and kinetic analysis revealed that Tyr270 is essential to couple the NADH oxidation with the ring-opening and enhance the ring-opening activity.

Chaiyen *et al.* have discussed the mechanism of substrate binding and subsequent NADH binding and hydride transfer (reductive half-reaction) in MHPCO (*2*,

6). They reported that MHPCO enhances the rate of hydride transfer several thousand-fold in the presence of a substrate, and this effector role of substrate does not change the redox potential of FAD or a thermodynamic driving force (*6*). They proposed that the substrate binding facilitates the binding of NADH to be in an optimum geometry for transferring a hydride ion to FAD. This proposal well agrees with the increase in turnover number (0.19 to 1300 s^{-1}) in the turnover number of the WT enzyme (Table II). The lack of change in the turnover numbers in the Y270F and Y270A mutants strongly suggested that Tyr270 is essential to make MHPC (or 5HN) to be the effector in the enzyme reaction. In the crystal structure of SeMet MHPCO/MHPC complex reported by McCulloch *et al.* (*3*), Tyr270 formed water-mediated hydrogen bonds with the C5 carboxyl group of MHPC (Fig. 3, right). In the present complex with 5PA, the side chain of Tyr270 took two conformations (Fig. 3, center). Both conformations of Oη formed a direct or a water-mediated hydrogen bond with the hydroxyl group at the C4 position of 5PA of the B conformation. The disturbed position of 5PA and Tyr270 in the 5PA complex may explain why MHPCO showed lower activity toward 5PA.

Although MHPCO belongs to the FAD-dependent monooxygenase superfamily and has catalytic mechanisms similar to the other family members, the enzyme shows different property in the reductive half-reaction. MHPCO does not use a conformational change of FAD or form a charge-transfer complex with NADH. Tyr270 may play a major role in these differences. To further elucidate the mechanism of the reductive half-reaction in MHPCO, The author is currently trying to determine the crystal structures of the MHPCO/5HN, mutants/5HN and MHPCO/NAD(H) complex.

References

1. Sparrow, L. G., Ho, P. P. K., Sundaram, T. K., Zach, D., Nyns, E. J., and Snell, E. E. (1969) *J. Biol. Chem.* **244**, 2590-2600.
2. Chayien, P. (2009) *Arch*. *Biochem*. *Biophys*. **493**, 62-70.
3. McCulloch, K.M., Mukherjee, T., Begley, T.P., and Ealick, S.E. (2009) *Biochemistry* **48**, 4139-4149
4. Kishore, M. G., and Snell, E. E. (1981) *J. Biol. Chem.* **256**, 4228-4233.
5. Yuan, B., Yoshikane, Y., Yokochi, N., Ohnishi, K., and Yagi, T. (2004) *FEMS Microbiol. Lett.* **234**, 225-230.
6. Chaiyen, P., Brissette, P., Ballou, D.P., and Massey, V. (1997) *Biochemistry* **36**, 2612-2621
7. Yokochi, N., Yoshikane, Y., Matsumoto, S., Fujisawa, M., Ohnishi, K., and Yagi, T. (2009) *J. Biochem*. **145**, 493-503
8. Otwinowski, Z., and Minor, W. (1997) *Methods Enzymol.* **276**, 307-326
9. Vagin, A., and Teplyakov, A. (1997) *J. Appl. Cryst.* **30**, 1022-1025
10. Winn, D.M., Ballard, C.C., Cowtan, D.K., Dodson, J.E., Emsley, P., Evans, R.P., Keegan, M.R., Krissinel, B.E., Lesile, W.G.A., McCoy, A., McNicholas, J.S., Murshudov, N.G., Pannu, S.N., Potterton, A.E., Powell, R.H., Read, J.R., Vagin, A., and Wilson, S.K. (2011) *Acta. Crystallogr.* D**67**, 235-242
11. Murshudov, N.G., Vagin, A.A., and Dodson, J.E. (1996) *Acta. Crystallogr.* D**53**, 240-255
12. Adams, D.P., Afonine, V.P., Bunkoczi, G., Chen, B.V., Davis, W.I., Echols, N., Headd, J.J., Hung, -W.L., Kapral, J.G., Grosse-Kunstleve, W.R., McCoy, J.A., Moriarty, W.N., Oeffner, R., Read, J.R., Richardson, C.D., Richardson, S.J., Terwillger, C.T., and

Zwart, H.P. (2010) *Acta. Crystallogr.* D**66**, 213-221

13. Emsley, P., and Cowtan, K. (2004) *Acta. Crystallogr.* D**60**, 2126-2132
14. Schuttelkopf, W.A., and Aalten van, F.M.D. (2004) *Acta. Crystallogr.* D**60**, 1355-1363
15. Laskowski, A.R., MacArthur, W.M., Moss, S.D., and Thornton, M.J. (1993) *J. Appl. Cryst.* **26**, 283-291
16. Vaguine, A.A., Richelle, J., and Wodak, S.J. (1999) *Acta. Crystallogr.* D**55**, 191-205
17. Krissinel, E., and Henrick, K. (2007) *J. Mol. Biol.* **372**, 774-797
18. Ramachandran, G. N., and Sasisekharan, V. (1968) *Adv. Protein Chem.* **23**, 283-438

Chapter 3

Crystal Structure of α-(*N*-Acetylaminomethylene) Succinic Acid Amidohydrolase

Introduction

α-(*N*-Acetylaminomethylene) succinic acid amidohydrolase (AAH) catalyzes degradation of AAMS to acetate, ammonia, carbon dioxide and succinic semialdehyde. The enzymatic property of AAH from *M. loti* has been reported (*1*). The enzyme is a homodimeric protein with a molecular weight of 64,000 (subunit: 32,000), and exhibits K_m and k_{cat} values of 54.0 μM and 5.2 s^{-1}, respectively. The catalytic residues are thought to be a typical catalytic triad, Ser-His-Asp found in many serine proteases. The primary structure of the enzyme did not show significant identity to any hydrolase, but it showed low but significant homology with several esterases and dehalogenases (Fig. 1). Based on the sequence alignment, the catalytic residues of AAH can be predicted to be Ser106 and His258 residues. However, the catalytic Asp residue cannot be predicted. Therefore, AAH has not been assigned to any enzyme family and the catalytic mechanism has not been elucidated. The crystal structure of SeMet AAH has recently been determined and the structural feature, catalytic residues and catalytic mechanism have been discussed (*2*). However, the enzyme has not been assigned into an enzyme family properly.

In this chapter, I describe the determination of the crystal structure of WT AAH at 2.7 Å resolution, and propose presence of a new subclass in the α/β hydrolase

superfamily based on BLAST search and CLUSTALW.

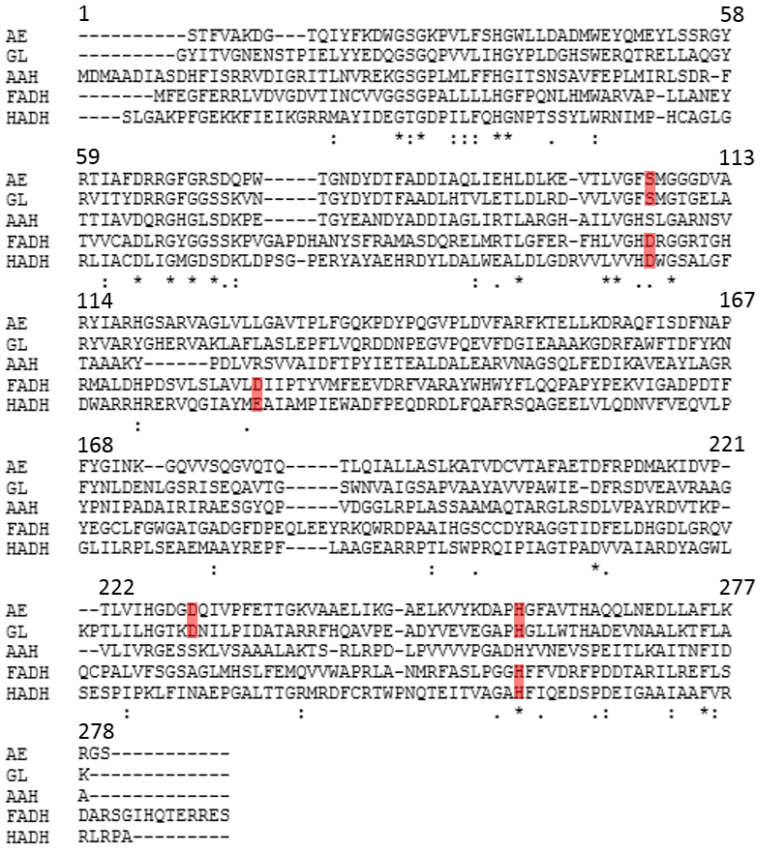

Figure 1. Sequence alignment of AAH with several esterases and dehalogenases. AE, aryl esterase from *Pseudomonas fluorescens*; GL, γ-lactamase from *Aureobacterium* sp.; FADH, fluoroacetate dehalogenase from *Burkholderia* sp.; HADH, haloalkane dehalogenase from *Sphingomonas paucimobilis*. Numbers of amino acid residues from N-terminal in AAH are shown. Catalytic residues of the esterases and dehalogenases are shown in red.

Materials and Methods

Protein and enzyme assay

The activity of AAH was measured as reported previously (*1*). Protein concentration was measured by a Bio-Rad Protein Assay (Bio-Rad) using bovine serum albumin as a standard. The concentration of purified AAH was determined from the molecular absorption coefficient (ε = 23,040 $M^{-1}cm^{-1}$) at 280 nm (*1*).

Purification of WT AAH

A bacterial strain, plasmid and reagents reported previously were used (*1*). The

method to induce the expression of WT AAH was also the same as described previously (*1*). The purification method of the enzyme was modified. The recombinant *E. coli* BL21 (DE3) cells were suspended in sonication buffer [50 mM KPB (pH 7.0), 14 mM 2ME, and 0.1 mM PMSF]. The suspension was sonicated on ice for 6 min using a W-220 sonicator (Heat Systems Ultrasonics). The first supernatant was obtained by centrifuging at 10,000 g for 20 min at 4^{o}C. The precipitant was resuspended in the sonication buffer, sonicated and centrifuged again. The second supernatant was mixed with the first supernatant to make a crude extract. The crude extract was fractionated with 40-55% saturated ammonium sulfate. The precipitant obtained after centrifugation was dissolved in Buffer A [50 mM KPB (pH 7.0), 0.1% 2ME]. The enzyme solution was applied to a Butyl-Toyopearl 650 M (Tosoh) column chromatography. The column was equilibrated with Buffer A containing 1 M ammonium sulfate, and then the sample was applied. The column was washed with Buffer A containing 1 M ammonium sulfate, and then the proteins bound to the column were eluted by a linear gradient with Buffer A. Fractions showing AAH activity were eluted around 0.4 M ammonium sulfate. The fractions were checked by SDS-PAGE, collected and concentrated by 0-55% saturated ammonium sulfate precipitation. After centrifugation, solubilization and dialysis with and against Buffer B [50 mM Tris-HCl (pH 7.0), 14 mM 2ME], the sample was applied to a hydroxyapatite (Nacalai Tesque, 100-200 mesh) column chromatography. The column was equilibrated with Buffer B and then the sample was applied. The column was washed with Buffer B, and then proteins bound to the column were eluted by a linear gradient with Buffer B supplemented with 50 mM KPB (pH 7.0). Fractions with the AAH activity were eluted around 10 mM KPB. The fractions were checked by SDS-PAGE, collected and concentrated by 0-55% saturated ammonium sulfate precipitation. After

centrifugation and solubilization with Buffer B, the sample was applied to a 5-diol-300II (Nacalai tesque) gel filtration column chromatography using Buffer B. The enzyme was eluted as a single peak, which corresponds to the AAH dimer. The purified enzyme was dialyzed against crystallization buffer [10 mM HEPES-NaOH (pH 7.0), 14 mM 2ME], and then used for crystallization.

Crystallization and structure analysis of WT AAH

The solution of WT AAH was ultra-filtered to 15 mg/ml by a VIVASPIN 20 (10,000 MWCO, Sartorius Stedim Biotech). The solution was applied to screening with Crystal Screen I and II (Hampton Research) and Wizard I and II (Emerald Biosystems) by the sitting-drop method at 4^{o}C and 20^{o}C. Although crystals of WT AAH were obtained by mixing equal volumes (2 μl) of the enzyme solution (12.5 mg/ml WT AAH in the crystallization buffer) and the reservoir solution [20% (w/v) PEG8000, 200 mM $MgCl_2$, 0.1 M Tris-HCl (pH8.5)] by the sitting drop method at 20^{o}C for 2 weeks, well-diffracted crystal was not obtained even after optimization (~7 Å resolution). Therefore, Additive Screen (Hampton Research) was then applied based on the reservoir solution. Better-diffracted crystals (~3 Å resolution) were obtained by mixing equal volumes (2 μl) of the enzyme solution (14 mg/ml WT AAH in the crystallization buffer) and the reservoir solution [18% PEG8000, 248 mM $MgCl_2$, 4% (v/v) 2,2,2-trifluoroethanol (TFE), 90 mM Tris-HCl (pH8.5)]. The best crystal of AAH (2.7 Å resolution) was obtained by additional streak seeding in the sitting drop method for 2 weeks at 20^{o}C using the better-diffracted crystal.

The crystal of WT AAH was picked up from a droplet and flash-cooled by a nitrogen-gas stream at -173^{o}C after quick soaking in a reservoir solution containing 30%

(v/v) glycerol. Diffraction data of the crystal were collected by synchrotron radiation with wavelength 1.0 Å at PF-AR NW12A of KEK. The data set were processed using HKL2000 (*3*). The phase was determined by a molecular replacement program, PHASER (*4*) in CCP4 (*5*), with SeMet AAH as a template (PDB ID: 3KXP) (*2*). After PHASER, The structure was refined by REFMAC5 (*6*) and PHENIX (*7*). Refinement by PHENIX and modeling by COOT (*8*) were repeated. Water molecules were added by COOT. The data collection and refinement statistics are shown in Table I. The buried solvent-accessible surface area of AAH was analyzed by PISA (*9*).

Table I. Data collection and refinement statistics.

	AAH
Data collection	
X-ray source	PF-AR NW12A
Wavelength (Å)	1.0000
Crystal system	Monoclinic
Space group	*C2*
Unit cell parameter (Å,°)	a = 393.230, b = 58.311, c = 98.897, β = 103.44,
Resolution limit (Å)	50-2.70 (2.80-2.70)
Measured reflections	162075 (16024)
Unique reflections	58555 (5935)
Redundancy	2.8 (2.7)
Completeness (%)	95.9 (97.5)
$< I/\sigma(I) >$	9.2 (2.6)
R_{merge} (%)	13.0 (31.3)
Refinement	
Resolution range (Å)	48.23-2.70 (2.74-2.70)
R-factor (%)	20.2 (24.8)
R_{free} (%)	27.3 (36.3)
Overall B value (Å^2)	51.66
No. of amino acid residue	268 × 7
No. of water	63

Values in parentheses are for the highest resolution shell.

Results and Discussion

Crystal structure of WT AAH

The initial phase of WT AAH was determined by the molecular replacement method, and then the structure was refined as shown in Table I. Ramachandran plots (*10*) of the structure showed that 91.8% of the amino acid residues existed in the most favored region, 5.8% in the allowed region and 2.4% in the disallowed region, respectively.

In the crystal structure of WT AAH, seven monomers (chains A-G) existed in the asymmetric unit, although the enzyme exists as a dimer in solution (*1*). A monomer (chain A) interacted with an adjacent monomer (chain B) at each C-terminal region (218-278 residues) (Fig. 2a, b). Several hydrogen bonds were formed between O of Thr219 and Nζ of Lys270* (3.3 Å), between Oδ2 of Asp247 and Nδ2 of Asn274* (3.0 Å), between N of Val250 and O of Val250* (3.0 Å), between O of Val250 and N of Val250* (3.0 Å), between Nζ of Lys270 and O of Thr219* (3.3 Å), and between Nδ2 of Asn274 and Oδ2 of Asp247* (3.0 Å). C-C contacts were also observed between Phe275 and Ala278* and between Ala278 and Phe275*. These interactions were also observed between chains C and D, and between chains E and F. Chain G was interacted with a symmetrical monomer, chain G* by the same manner. The buried solvent-accessible surface area per monomer by this dimerization was ~900 $Å^2$ (~8.5% of the whole area) by PISA (*9*). This interaction manner was also observed in the SeMet structure (*2*). Because 368-4746 $Å^2$ is considered to be reasonable for formation of a functional dimer (*11*), this dimer (~1800 $Å^2$) may represent a functional dimer in solution phase.

The overall structure of WT AAH monomer was consisted of an α/β hydrolase fold domain (11-136 and 209-278 residues) and a cap domain (137-208 residues) (Fig. 2c) as reported in the SeMet structure (*2*): the α/β hydrolase fold domain was consisted of central eight-stranded mixed β-sheet and six α-helices which sandwiched the β-sheet. The cap domain was consisted of four α-helices and 2-stranded antiparallel β-sheet. No major structural difference was observed between the WT and the SeMet structure (RMSD = 0.208 Å). The monomeric structure of WT AAH was also similar to several dehalogenases and esterases as shown in ref. (*2*).

Catalytic residues deduced from the sequence alignment (*1*), Ser106 and His258

were located between the domains (Fig. 2c, d). A hydrogen bond was observed between Oγ of Ser106 and Nε2 of His258 (2.8 Å). Nδ1 of His258 also formed a hydrogen bond with Oδ2 of Asp130 (2.7 Å) to form a typical catalytic triad observed in hydrolases. A possible oxyanion hole occupied by a water molecule was formed by N of Ile41 and N of Leu107. Although further site-directed mutagenesis and kinetic experiments are needed, the catalytic triad of AAH was suggested to be Ser106-Asp130- His258 corresponding to the catalytic triad found in many serine proteases.

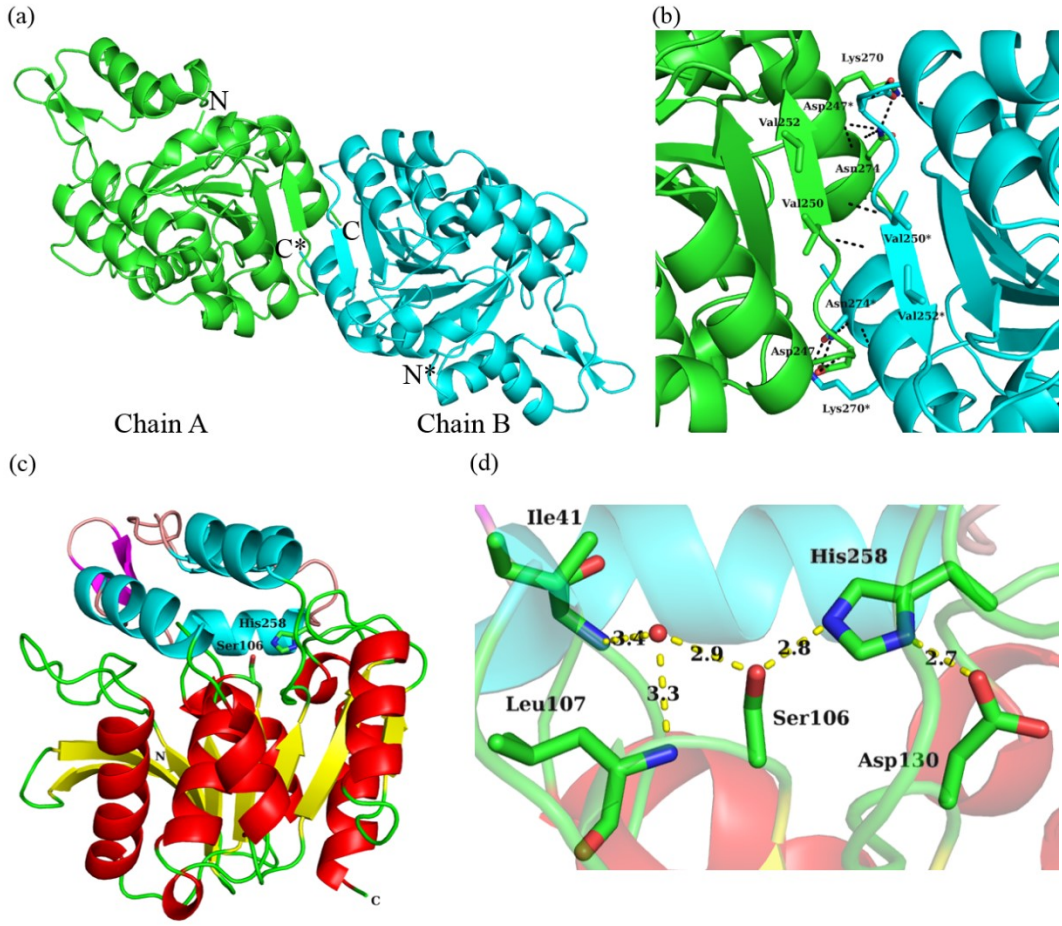

Figure 2. Crystal structure of AAH. (a) A possible dimer of AAH. Chains A and B in an asymmetrical unit are colored green and cyan, respectively. N- and C-terminals are labeled as N and C, respectively. (b) The dimeric interface enlarged from the same direction in (a). Amino acid residues involved in the dimerization are shown as stick models. Hydrogen bonds are shown as black broken lines. (c) Monomeric structure of AAH. α-Helices, β-strands and loops in the α/β fold domain are colored in red, yellow and green, respectively. α-Helices, β-strands and loops in the cap domain are colored in cyan, magenta and pink, respectively. Possible catalytic residues are shown as sticks. (d) A possible catalytic triad and oxyanion hole. The active site is enlarged from the same direction in (c). Catalytic triad, Ser106-Asp130-His258 is shown as sticks. Ile41 and Leu107 are also shown as sticks. A water molecule is shown as red sphere. A possible oxyanion hole is occupied by the water molecule. Hydrogen bonds are shown as yellow broken lines with their distances.

Assignment of AAH to a new subclass in the α/β hydrolase superfamily

The catalytic residues of AAH were assumed to be the typical catalytic triad found in many serine proteases. Comparison of the arrangement of the catalytic residues

in the primary structures (Fig. 1) showed that AAH was similar to dehalogenases than to esterases: the location of Asp residue in AAH and dehalogenases were at ~130 from the N-terminals, whereas that of esterases were at ~230. Combining with the phylogenic tree (*1*), these results suggest that AAH evolutionarily occupies the location of the middle of the esterases and dehalogenases. BLAST search showed that the primary structure of AAH is 25-96% identical with 98 proteins, such as WP_019860101.1 from *Mesorhizobium loti* (96% identity), YP_007303897.1 from *Mesorhizobium australicum* WSM2073 (89%), WP_018063448.1 from *Martelella mediterranea* (77%), WP_018851565.1 from *Streptomyces* sp. CNY243 (47%), WP_010805511.1 from *Pandoraea* sp. SD6-2 (28%) and WP_009341556.1 from *Streptomyces ipomoeae* 91-03 (30%). Surprisingly, 62 proteins out of the 98 proteins have the same relative arrangement of Ser-Asp-His catalytic triad residues as that of AAH. The similarity was high all from N- to C-terminals (Fig. 3), showing that the tertiary structures of these proteins are also similar. Although all of the 62 proteins have not been characterized, AAH and these proteins may make a new subclass in the α/β hydrolase superfamily. The previous report (*2*) showed that AAH was similar to members of an esterase subclass of the α/β hydrolase superfamily. However, here, I would like to propose the presence of a new subclass in the superfamily to which AAH belongs.

In this chapter, I described the structural feature of WT AAH and the presence of the new subclass in the α/β hydrolase superfamily. Two catalytic mechanisms of AAH have been proposed (*2*). Site-directed mutagenesis and kinetic experiments and the structural determinations of AAH/substrate and AAH/intermediate complexes are needed to determine the catalytic mechanism of AAH.

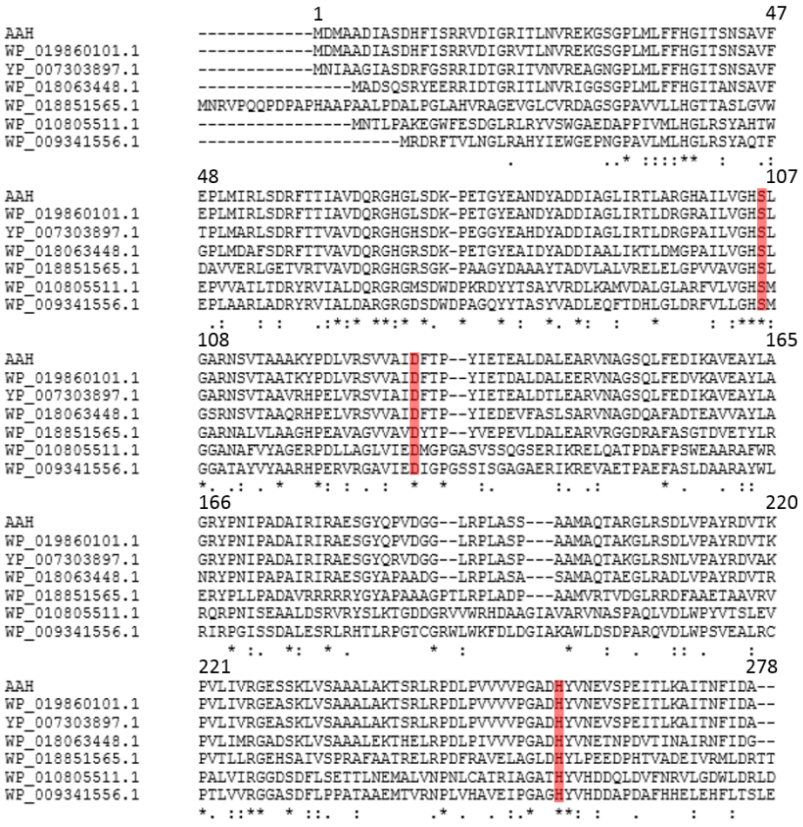

Figure 3. Sequence alignment of AAH with similar proteins. Numbers of amino acid residues from N-terminal in AAH are shown. Catalytic residues are shown in red.

References

1. Yuan, B., Yokochi, N., Yoshikane, Y., Ohnishi, K., Ge, F., and Yagi, T. (2008) *J. Nutri. Sci. Vitaminol. (Tokyo)* **54**, 185-190.
2. McCulloch, K. M., Mukherjee, T., Begley, T. P., and Ealick, S. E. (2010) *Biochemistry* **49**, 1226-1235
3. Otwinowski, Z., and Minor, W. (1997) *Methods Enzymol.* **276**, 307-326
4. McCoy, A. J., Grosse-Kunstleve, R. W., Adams, P. D., Winn, M. D., Storoni, L. C., and Read, J. (2007) *J. Appl. Cryst.* **40**, 658-674
5. Winn, D.M., Ballard, C.C., Cowtan, D.K., Dodson, J.E., Emsley, P., Evans, R.P., Keegan, M.R., Krissinel, B.E., Lesile, W.G.A., McCoy, A., McNicholas, J.S., Murshudov, N.G., Pannu, S.N., Potterton, A.E., Powell, R.H., Read, J.R., Vagin, A.,

and Wilson, S.K. (2011) *Acta. Crystallogr.* D**67**, 235-242

6. Murshudov, N.G., Vagin, A.A., and Dodson, J.E. (1996) *Acta. Crystallogr.* D**53**, 240-255
7. Adams, D.P., Afonine, V.P., Bunkoczi, G., Chen, B.V., Davis, W.I., Echols, N., Headd, J.J., Hung, -W.L., Kapral, J.G., Grosse-Kunstleve, W.R., McCoy, J.A., Moriarty, W.N., Oeffner, R., Read, J.R., Richardson, C.D., Richardson, S.J., Terwillger, C.T., and Zwart, H.P. (2010) *Acta. Crystallogr.* D**66**, 213-221
8. Emsley, P., and Cowtan, K. (2004) *Acta. Crystallogr.* D**60**, 2126-2132
9. Krissinel, E., and Henrick, K. (2007) *J. Mol. Biol.* **372**, 774-797
10. Ramachandran, G. N., and Sasisekharan, V. (1968) *Adv. Protein Chem.* **23**, 283-438
11. Jones, S., and Thornton, J. M. (1996) *Ploc. Natl. Acad. Sci. U.S.A. 93*, 13-20

Conclusions

1. The crystal structures of 4-pyridoxolactonase and its complex with 5PAL were determined. Combining with the results of the docking simulations, it was found that the enzyme catalyzes the reaction through the subclass B2-like mechanism of class B β-lactamase (the dianion intermediate), not the subclass B3 mechanism (the anionic oxygen intermediate) to which 4-pyridoxolactonase belongs.

2. The crystal structures of the WT MHPCO and its complex with 5PA were determined. In the MHPCO/5PA complex, Tyr270 took two conformations by the two conformations of C4 hydroxymethyl group of 5PA. The site-directed mutagenesis and kinetic analyses revealed that Tyr270 is essential to enhance the rate of the reductive-half reaction.

3. The crystal structure of WT AAH was determined at 2.7 Å resolution. The structure strongly suggested that catalytic residues of AAH involve a typical catalytic triad, Ser106-Asp130-His258 observed in many serine proteases. This arrangement of the catalytic triad was observed for the first time in the α/β hydrolase superfamily. BLAST search strongly suggested that the presence of a new subclass shared the same arrangement of the catalytic triad in the α/β hydrolase superfamily.

Acknowledgements

The author is deeply indebted to Dr. Toshiharu Yagi for his kind guidance and warm encouragement during this study.

The author is greatly indebted to Dr. Shigehiro Kamitori, Professor of Faculty of Medicine, Kagawa University and Dr. Hiromi Yoshida, Associate Professor of Faculty of Medicine, Kagawa University for their warm and helpful collaborations.

The author is grateful to Dr. Bunzo Mikami, Professor of Graduate School of Agriculture, Kyoto University, Dr. Nobuyuki Takahashi, Assistant Professor of Graduate School of Agriculture, Kyoto University and Dr. Kimihiko Mizutani, Assistant Professor of Graduate School of Agriculture, Kyoto University for their valuable suggestions and helps.

Thanks are given to all the members of the Laboratories of Applied Biochemistry, Graduate School of Integral Arts and Science, Kochi University and of Applied Structural Biology, Graduate School of Agriculture, Kyoto University.

Jun Kobayashi

List of Publications

Original papers

1. Jun Kobayashi, Yu Yoshikane, Toshiharu Yagi, Seiki Baba, Kimihiko Mizutani, Nobuyuki Takahashi and Bunzo Mikami. (2014). Structure of 4-pyridoxolactonase from *Mesorhizobium loti*. *Acta. Crystallogr. Sect. F Struct. Biol. Cryst. Commun.* **70**, 424-432.
2. Jun Kobayashi, Hiromi Yoshida, Toshiharu Yagi, Shigehiro Kamitori, Hideyuki Hayashi, Kimihiko Mizutani, Nobuyuki Takahashi and Bunzo Mikami. (2014). Role of Tyr270 in 2-Methyl-3-hydroxypyridine-5-carboxylic acid oxygenase from *Mesrhizobium loti*. in preparation.
3. Jun Kobayashi, Hiromi Yoshida, Huy Nhat Chu, Yu Yoshikane, Shigehiro Kamitori and Toshiahru Yagi. (2009). Crystallization and preliminary X-ray analysis of AAMS amidohydrolase, the final enzyme in degradation pathway I of pyridoxine. *Acta. Crystallogr. Sect. F Struct. Biol. Cryst. Commun.* **65**, 829-831.

Related papers

1. Sayoko Matsuda, Nana Yokochi, Yu Yoshikane, Jun Kobayashi, Chu Nhat Huy, Seiki Baba, Seiki Kuramitsu, Bunzo mikami and Toshiharu Yagi. (2009). Crystallization and preliminary X-ray analysis of 4-pyridoxolactonase from *Mesorhizobium loti*. *Acta. Crystallogr. Sect. F Struct. Biol. Cryst. Commun.* **65**, 886-889.
2. Huy Nhat Chu, Jun Kobayashi, Yu Yoshikane, Bunzo Mikami and Toshiharu Yagi. (2010). Crystallization and preliminary X-ray analysis of SDR-type pyridoxal

dehydrogenase from *Mesorhizobium loti*. *Acta. Crystallogr. Sect. F Struct. Biol. Cryst. Commun.* **66**, 718-720.

3. Huy Nhat Chu, Jun Kobayashi, Bunzo Mikami and Toshiharu Yagi. (2010). Crystal structure of SDR-type pyridoxal 4-dehydrogenase from *Mesorhizobium loti*. *Biosci. Biotecnol. Biochem.* **75**, 388-390.
4. Andrew Njagi Mugo, Jun Kobayashi, Bunzo Mikami, Kouhei Ohnishi and Toshiharu Yagi. (2012). Crystallization and preliminary X-ray analysis of pyridoxine 4-oxidase, the first enzyme in pyridoxine degradation pathway I. *Acta. Crystallogr. Sect. F Struct. Biol. Cryst. Commun.* **68**, 66-68.
5. Andrew Njagi Mugo, Jun Kobayashi, Taiji, Yamasaki, Bunzo Mikami, Kouhei Ohnishi and Toshiharu Yagi. (2013). Crystal structure of pyridoxine 4-oxidase from *Mesorhizobium loti*. *Biochim. Biophys. Acta* **1834**, 953-963.